Using Colour Image Segmentation with Magnetic Resonance Images for Computed Tomography Synthesis

Jules Faucher

Medical Physics Unit

McGill University, Montreal

August 2024

A thesis submitted to McGill University in partial fulfillment of the requirements for the degree of *Master of Science in Medical Radiation Physics*

Table of Contents

List of Figures

List of Tables

List of Abbreviations

AI	Artificial Intelligence
CBCT	Cone Beam Computed Tomography
CIELAB	Commission Internationale de l'Éclairage L* a* b*
CSF	Cerebrospinal Fluid
CT	Computed Tomography
CTV	Clinical Target Volume
DSC	Dice Similarity Coefficient
EBRT	External Beam Radiation Therapy
FA	Flip Angle
FCM	Fuzzy-C-Means
FOV	Field of View
GAN	Generative Adversarial Networks
GRE	Gradient (Recall) Echo
GTV	Gross Tumour Volume
HU	Hounsfield Unit
ICC	IntraClass Correlation
MAE	Mean Absolute Error
mDixon	Multi-point Dixon
ME	Mean Error
MPRAGE	Magnetization Prepared Rapid Gradient Echo
MR	Magnetic Resonance
MRI	Magnetic Resonance Imaging
MV	Megavoltage
OAR	Organs at risk
PD	Proton Density
PDw	Proton Density-weighted

PET	Positron Emission Tomography
PNS	Peripheral Nerve Stimulation
PTV	Planning Target Volume
QSM	Quantitative Susceptibility Mapping
RAG	Region Adjacency Graph
RED	Relative Electron Density
RGB	Red-Green-Blue
RT	Radiation Therapy
RTP	Radiotherapy Treatment Planning
sCT	Synthetic Computed Tomography
STD	Standard Deviation
SLIC	Simple Linear Iterative Clustering
T1w	T_1-weighted
T2w	T_2-weighted
TE	Echo Time
TR	Repetition Time
UTE	Ultra-short Echo Time
ZTE	Zero Echo Time

Abstract

Mostly known for its use in cancer care, radiotherapy is a treatment modality that uses ionizing radiation to kill malignant cells. This form of therapy requires careful planning that for nearly three decades has been based on computed tomography (CT) images, from which the position of tumours and healthy tissues can be determined. However, CT alone cannot always provide the contrast necessary to define targets. In these cases, the superior soft tissue contrast of magnetic resonance imaging (MRI) is used for more reliable contouring. Unfortunately, MRI alone is insufficient for treatment planning because CT images are also used to estimate a map of the electron density of patients, enabling accurate dose calculations. To eliminate the need for two different scans, CT images could be replaced by synthetic CT (sCT) images produced using MRI.

CT synthesis from MRI is challenging because bone and air are typically indistinguishable in MR images. While air produces very little signal per volume, the signal produced by bone decays far too rapidly to be measured using conventional MRI pulse sequences. Bone visibility can be achieved with ultra-short echo time (UTE) imaging, but this information alone is insufficient to segment the different tissues relevant to CT and assign adequate pixel values in the sCT. Hence, CT synthesis algorithms often rely on multiple different MR images acquired over sometimes lengthy scan times and combined with elaborate algorithms that may rely on assumptions about the anatomy of patients. Other approaches based on artificial intelligence can exploit conventional MR images but must be trained on large datasets to perform well. This complicates their adaptation to different anatomical sites and can limit their accuracy on patients whose atypical anatomies were not well represented in training datasets.

This work presents a novel method based on UTE MR imaging that does not rely on assumptions about the anatomies of patients. Three rapidly acquired MR images with different contrasts are merged to create a colour image. Different tissues are then distinguished and identified based on their colour. Pixel values can then be assigned to the sCT based on tissue type. This algorithm was tested on images of a phantom and of the heads of human volunteers. The results suggest that our method can accurately differentiate between air and bone and subsequently generate sCT images with plausible appearance. However, errors in the segmentation of fat suggest that the algorithm or the acquisition could be further improved.

Résumé

Principalement connue pour son utilisation dans les soins contre le cancer, la radiothérapie est une méthode de traitement qui utilise des rayons ionisants pour détruire les cellules malignes. Cette forme de thérapie nécessite une planification minutieuse qui, depuis près de trois décennies, est basée sur des images de tomodensitométrie (TDM), à partir desquelles la disposition des tumeurs et des tissus sains peut être déterminée. Cependant, la TDM seule ne peut pas toujours fournir le contraste nécessaire afin de bien définir les cibles. Dans ces cas, le contraste supérieur des tissus mous de l'imagerie par résonance magnétique (IRM) est utilisé pour une délimitation plus fiable. Malheureusement, l'IRM seule est insuffisante pour la planification du traitement car les images de TDM sont également utilisées pour générer une carte estimative de la densité électronique des patients, permettant des calculs de dose précis. Pour éliminer le besoin de deux scans différents, les images de TDM pourraient être remplacées par des images de TDM synthétiques (TDMs) produites à partir de l'IRM.

La synthèse de TDM à partir de l'IRM est difficile car l'os et l'air sont généralement indiscernables sur les images d'IRM. Alors que l'air produit très peu de signal, le signal produit par l'os se dégrade trop rapidement pour être mesuré à l'aide des séquences d'impulsion d'IRM conventionnelles. L'imagerie à temps d'écho ultra-court (UTE, d'*ultra-short echo time*) peut rendre les os visibles, mais par elle-même cette information est insuffisante pour segmenter les différents tissus pertinents en TDM et attribuer des valeurs adéquates aux pixels du TDMs. Ainsi, les algorithmes de synthèse de TDM s'appuient souvent sur plusieurs images d'IRM différentes, acquises sur de longues durées et combinées avec des algorithmes élaborés qui peuvent se fier sur des suppositions concernant l'anatomie des patients. D'autres approches basées sur l'intelligence artificielle peuvent exploiter des images d’IRM conventionnelles mais doivent être entraînées sur de grands ensembles de données pour bien fonctionner. Cela complique leur adaptation à différents sites anatomiques et peut limiter leur précision sur des patients dont les anatomies atypiques ne sont pas bien représentées dans les ensembles de données d'entraînement.

Ce travail présente une méthode novatrice basée sur l'imagerie UTE qui ne repose sur aucune supposition concernant l’anatomie des patients. Trois images d’IRM acquises rapidement avec différents contrastes sont fusionnées pour créer une image en couleur. Les tissus sont ensuite différentiés et identifiés en fonction de leur couleur. Les valeurs des pixels peuvent ensuite être attribuées au sCT en fonction du type de tissu. Cet algorithme a été testé sur des images d'un fantôme et des têtes de volontaires humains. Les résultats suggèrent que notre méthode peut différencier correctement l'air et l'os pour ensuite générer des images sCT d'apparence plausible. Cependant, des erreurs dans la segmentation des tissus adipeux suggèrent que l'algorithme ou l'acquisition pourraient encore être améliorés.

Acknowledgements

First and foremost, I want to thank my supervisor Prof. Ives Levesque for giving me the opportunity to freely explore the world of MRI under his guidance. His advice and teaching have led me to create the project that I am proud of presenting in this thesis.

I want to thank everyone who made the phantom experiments possible, Joe Larkin, Boucherie Vito, and Titanium Industries, for experimental materials, Renée-Claude Bider and Jorge Campos Pazmino for their assistance in building phantoms, Emily Poon and Peter Watson for CT scans, and Paule Marcoux-Valiquette and Evan McNabb for MRI scans.

I also want to recognize that my scans would not have been possible without the Montreal General Hospital MRI Research Platform, the McGill University Health Center, Siemens Healthineers, and Philips Healthcare.

Beyond the lab, I want to express my gratitude towards my friends and family for their support and for sitting through my ramblings about spiral MRI over the past year.

Finally, I want to acknowledge the financial support I received from the "Fonds de recherche en nature et technologies de Québec" through the *Bourse de maîtrise en recherche* award. I also received funding thanks to the *Bourse Établissement de jeune chercheur* from the "Fonds de recherche en santé du Québec", the *Discovery Grant* from the National Science and Engineering Research Council of Canada, and funding from the Montreal General Hospital Foundation that were secured by Prof. Levesque.

Contribution of Authors

Jules Faucher, the author of this thesis, designed and carried out the experiments, developed the algorithm proposed in this work, analysed the results, wrote the text in this thesis, and created all the figures. Prof. Ives Levesque supervised the project, supported the experimental work and edited the contents of the thesis. Prof. Véronique Fortier and Mr Evan McNabb participated in discussing the image quality of MRI scans, and reviewed the manuscript presented in Chapter 4. Mr Evan McNabb also contributed to the pulse sequence protocol design.

Chapter 1: Introduction

1.1 Motivation

Radiotherapy (RT) is a family of treatments that use ionizing radiation to treat different ailments, typically cancer. Such treatments need to be planned to deliver the adequate amount of radiation to the lesion while avoiding the irradiation of normal tissues as much as possible[1]. Modern-day radiotherapy treatment planning (RTP) relies heavily on computed tomography (CT) to produce images that are used to define therapeutic targets and contour organs-at-risk (OAR). CT scanners acquire hundreds of X-ray projection images at kilovoltage energies to reconstruct cross-sectional images of the subjects scanned[2]. Since CT images are created using X-rays, the pixel values, often referred to as CT numbers and given in Hounsfield units (HU), contain information on the attenuation of radiation through the patient[3]. CT numbers can be used to estimate the electron density of tissues, which is used to calculate the dose to the patient, allowing for the optimization of the treatment[3].

Unfortunately, CT has limited soft tissue contrast and magnetic resonance (MR) images may be necessary for proper target delineation in a number of applications[4]. MR imaging (MRI) offers a wide range of contrasts, but never directly depends on electron density. Hence, MRI alone cannot be used for dose calculations, and CT images are still needed for this task[4]. In many cases, patients undergo CT and MRI, which are then registered. The potential misalignment of these images can lead to errors in the treatment plan[5]. Furthermore, the need to simulate the treatment on both scanners requires a substantial amount of time, burdening the healthcare system[6].

Synthesizing CT images using MRI has been considered a potential solution towards MR-only simulation by many researchers[4]. In addition to lowering the uncertainty in treatment plans and streamlining the clinical workflow, eliminating CT in favour of MRI would contribute to lowering the dose to healthy tissues. Several approaches have been developed for CT synthesis, without a clear consensus on the best method and a limited number of commercially available software products[7-9]. CT synthesis remains an open question.

1.2 Objectives

A previously proposed algorithm for sCT from our group relies on quantitative magnetic susceptibility (QSM) to differentiate bone from air, and fat-water separation to characterize the composition of soft tissues[10]. Information from both analyses were combined to compute CT numbers for each voxel of the MR images. While promising, this approach has a lengthy image acquisition, and the algorithm for sCT is complicated and relies on morphological operations that may be invalid in other sites than the head. To address these issues, a new approach was developed around ultra-short echo time (UTE) imaging, a family of specialized MRI pulse sequences that allows direct imaging of bone[11].

The first objective of this project was to develop an acquisition protocol using a spiral sequence for UTE imaging, with the benefit of higher sampling efficiency to achieve shorter scan times.

The second goal was to achieve the segmentation of tissues relevant to CT synthesis on MR images. Red-green-blue (RGB) images were constructed from three MRI scans with different contrast by assigning these to the colour channels. On these multi-channel images, different tissues have different colours. This allows the use of well-established deterministic colour image segmentation algorithms, which were primarily developed to segment so-called “natural images” (colour pictures obtained with the every-day camera) to potentially produce tissue segmentations. One combination of algorithms— simple linear iterative clustering[12] paired with region adjacency graph thresholding[13]—was tested in this work.

The final objective was to use the segmentation of the tissues present on these combined MR images to assign CT numbers to the sCT and to test this novel method both in a phantom and *in vivo*. Synthetic CT and X-ray CT images were compared quantitatively in a phantom featuring materials of interest, including water-based gel (as a proxy for water-based tissue), plastic, pieces of bovine femur, air cavities, and fatty bone marrow. Then, three volunteers were scanned for their sCT images to be evaluated qualitatively.

1.3 Thesis Outline

The second chapter of this work, “Background”, provides the reader with an overview of the physics of MRI, colour image segmentation, and treatment planning in radiation therapy. Chapter 3, “Literature Review”, surveys recent publications on the topic of CT synthesis and dives into different successful approaches. Chapter 4 presents a manuscript which describes the methods and results of this research project, to be submitted for publication. Chapter 5 further discusses and generalizes the implications of our results, design decisions, and potential improvements to the acquisitions and segmentation. Chapter 6 concludes this thesis with a summary of our results and describes prospective research avenues that could improve the accuracy of our novel CT synthesis method.

Chapter 2: Background

2.1 Principles of Magnetic Resonance

MRI is an imaging modality that relies on the interaction between nuclear spins and magnetic fields to produce images. This is most accurately described by quantum mechanics, yet classical theory is sufficient to describe most principles of MRI. The theory presented in Sections 2.1 and 2.2 are based on the textbook by McRobbie *et al.*[14]

2.1.1 Nuclear Magnetic Resonance

Nucleons exhibit an intrinsic magnetic moment and angular momentum (or *spin*). Within the nucleus, nucleon spins align anti-parallel to minimize energy. A nucleus with an even number of nucleons has no net spin, and an odd number of nucleons generates a half-integer spin.

In a magnetic field ($\vec{B}$), nuclei with half-integer spins align themselves with the field in the parallel or anti-parallel direction. For simplicity, this work only considers such nuclei, as net zero spin yields no interaction. Depending on the magnitude of $\vec{B}$ and on the temperature, more spins will align parallel to $\vec{B}$, thus creating a net magnetization $\vec{M}$. MRI systems produce a strong main magnetic field (B_0) to magnetize the tissues of patients.

A misalignment between $\vec{M}$ and $\vec{B}$ results in a torque on the net magnetization, causing $\vec{M}$ to precess around $\vec{B}$. The angular frequency of the precession ω is equal to the magnitude of the magnetic field B scaled by the gyromagnetic ratio γ, per the Larmor equation:

$$\omega = \gamma B \qquad 2.1.1.1$$

The gyromagnetic ratio depends on the nuclei. It is equal to $2\pi \cdot 42.57 \times 10^6$ radians/s/T for hydrogen, the most common spin ½ nucleus in the human body, and therefore of interest in medical applications of MRI. The magnetization eventually realigns itself with $\vec{B}$ through a process of relaxation, covered in Section 2.1.2.

2.1.2 Excitation, Signal Detection, and Relaxation

Circularly polarized magnetic fields (B_1) oscillating at a frequency ω can be used to exert a torque on $\vec{M}$ and break its alignment from the main field. By adjusting the magnitude and duration of B_1 pulses, $\vec{M}$ can be tipped by a desired angle, called the flip angle (FA). B_1 pulses are achieved in MRI scanners by using transmit coils.

Following the B_1 excitation pulse, $\vec{M}$ undergoes gyroscopic precession. The resulting rotating dipole generates a time-varying magnetic field oscillating at the Larmor frequency. MRI scanners detect oscillations in $\vec{M}$ through magnetic induction in receiver coils, which may or may not be the same as the transmit coil depending on the scanner design and exam setup. Hence, the component of $\vec{M}$ transverse to B_0 generates the MRI signal.

While undergoing precession, the particles making up $\vec{M}$ dissipate their energy to their environment and realign themselves to B_0 through a process of relaxation. At the macroscopic scale, relaxation is described by longitudinal and transverse components best described by exponential recovery and decay functions, respectively.

Longitudinal relaxation is often referred to as T_1 relaxation in reference to the name of the variable that describes the time required for the longitudinal magnetization to recover 63% $(1 - e^{-1})$ of its equilibrium value. T_1 relaxation is promoted by spin-lattice coupling, where spins transfer energy to their environment.

Transverse relaxation is known as T_2 relaxation, which is the variable describing the time required for post-excitation transverse magnetization to decay by 63%. It is caused by the gradual dephasing of neighboring spins caused by spin-spin coupling occurring between the magnetic fields of nearby nuclei.

Other static effects can cause transverse relaxation to be faster than described by T_2. These effects are generally related to main field inhomogeneities that can be caused by patient-induced magnetic susceptibility inhomogeneities or machine specific imperfections. This faster decay is described by T_2*. Certain MRI techniques can be used to reverse these static effects and recover pure T_2 decay.

2.2 Gradients and Spatial Encoding

MRI systems can use a magnetic field varying linearly with space to create spatial variations in ω, thus encoding the position of spins along the gradient field in their Larmor frequency. Applying multiple perpendicular gradients at the same time results in a single gradient with an arbitrary direction. This implies that spatial encoding in more than one dimension must be executed in multiple steps, through time varying gradient fields.

The time domain interpretation of spatial encoding considers the effect of successive gradient pulses. For example, in 2D imaging, simultaneous excitation and gradient pulses excite a single cross-sectional *slice* of the patient. Then, prior to acquisition, a second short gradient field pulse is applied perpendicular to the first to encode one spatial dimension into the signal *phase*. Finally, a third gradient field, perpendicular to other two, is used to encode the final spatial dimension into the *frequency* of the signal. This process is repeated for different phase encodings, with identical excitations and frequency encodings. The series of magnetic field pulses is called a *pulse sequence*. The encoded signals are used to reconstruct the image. The interpretation of spatial decoding is straightforward using the Fourier transform (section 2.2.1).

2.2.1 k-Space Interpretation

It is easier to understand how gradient fields affect the spins of a sample by visualizing a point moving along a trajectory in the Fourier domain of the image, otherwise known as k-space. The demodulated signal as a function of time $S(t)$ for a spoiled gradient echo (GRE) sequence is given by Equation 2.2.1.1,

$$S(t) = \int_{\mathcal{V}} PD(\vec{r}) \cdot \left(\frac{1 - e^{-\frac{\mathrm{TR}}{T_1(\vec{r})}}}{1 - e^{-\frac{\mathrm{TR}}{T_1(\vec{r})}} \cos(\mathrm{FA})} \right) \sin(\mathrm{FA})\, e^{-\frac{t}{T_2^*(\vec{r})}} e^{i\gamma \int_0^t \vec{G}(s) \cdot \vec{r}\, ds} d\vec{r} \qquad 2.2.1.1$$

where $PD(\vec{r})$ is the proton density as a function of space, $\vec{G}(s)$ are the gradient pulses over time, and TR is the time elapsed between successive excitations. Trajectories in k-space can be defined as a function of the gradients using the substitution presented in Equation 2.2.1.2 to derive Equation 2.2.1.3.

$$\vec{k}(t) = \frac{\gamma}{2\pi} \int_0^t \vec{G}(s) ds \qquad 2.2.1.2$$

This substitution reveals that the signal exists in k-space, implying that the image is obtained by applying an inverse Fourier transform on the k-space data.

$$S(t) = \int_{V} PD(\vec{r}) \cdot \left(\frac{1 - e^{-\frac{\mathrm{TR}}{T_1(\vec{r})}}}{1 - e^{-\frac{\mathrm{TR}}{T_1(\vec{r})}} \cos(\mathrm{FA})} \right) \sin(\mathrm{FA})\, e^{-\frac{t}{T_2^*(\vec{r})}} e^{i2\pi\vec{k}(t)\cdot\vec{r}} d\vec{r} \qquad 2.2.1.3$$

Because MRI scanners use digital data, the discrete Fourier transformation is used, and k-space is best represented by an array of numbers the same size as the final image. The data collection must satisfy the Nyquist criterion (i.e. the grid must be fully sampled) to ensure the successful reconstruction of the image. In cartesian sampling, the grid is typically filled row by row (Figure 1). In this illustration, each row is filled by sampling the radio frequency signal received over different repetitions.

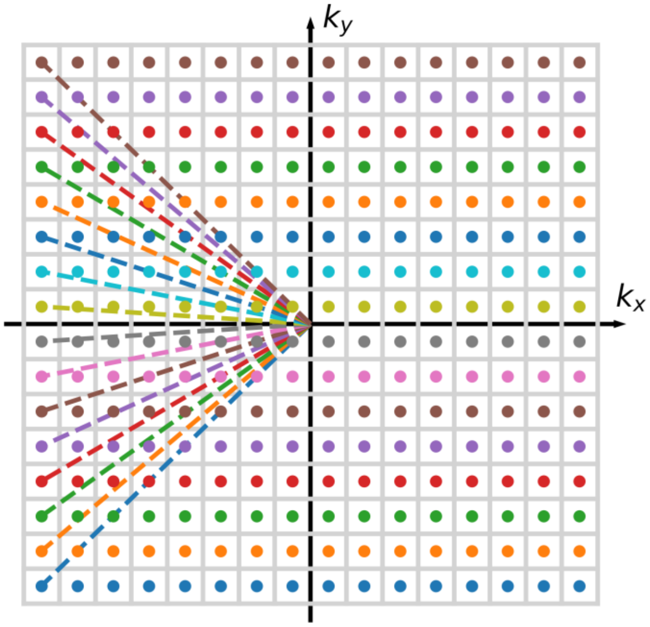

Figure 1: Common sampling scheme of k-space. Each color represents a different repetition. The dotted lines represent the phase encoding steps while the dots represent the samples acquired while the readout gradients are on.

2.3 Contrast in MRI

Contrast in MRI is mostly driven by proton density and relaxation rates. This section explains how three pulse sequence parameters – echo time (TE), repetition time (TR), and FA – are used to modify the signal intensity of tissues by manipulating relaxation, and subsequently control image contrast in MRI.

2.3.1 Echo Time

TE controls the time elapsed between excitation and the sampling of the center-most point in k-space. Increasing TE allows tissues to undergo T_2* relaxation in GRE sequences, and their signal to decay before sampling. In the final image, tissues with shorter T_2* appear darker than tissues with longer T_2*, an effect called T_2*-weighting. Figure 2 illustrates the decay of signals produced by a multi-echo GRE sequence for two different T_2*.

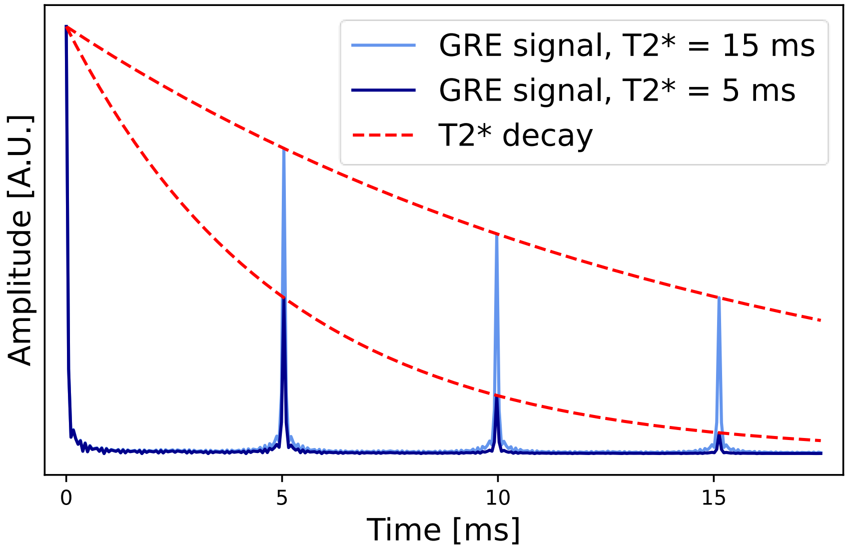

Figure 2: Intensity of a multi-echo gradient echo (GRE) signal over three echoes. This is the simulated signal of three echoes with 5-ms spacing (TE=5,10, and 15 ms, respectively).

2.3.2 Repetition Time

The time elapsed between successive excitations is controlled by TR. As seen in Figure 4a, a short TR in relation to T_1 causes an incomplete recovery of longitudinal magnetization before the next excitation. During a succession of 90° excitations converting all axial magnetization to transverse magnetization, longer T_1 species have less transverse magnetization to produce signal (Figure 3b), leading to T_1 contrast. Shortening TR further exacerbates this effect (Figure 3c). In summary, reducing TR darkens tissues with long T_1 on MR images, a phenomenon referred to as T_1-weighting.

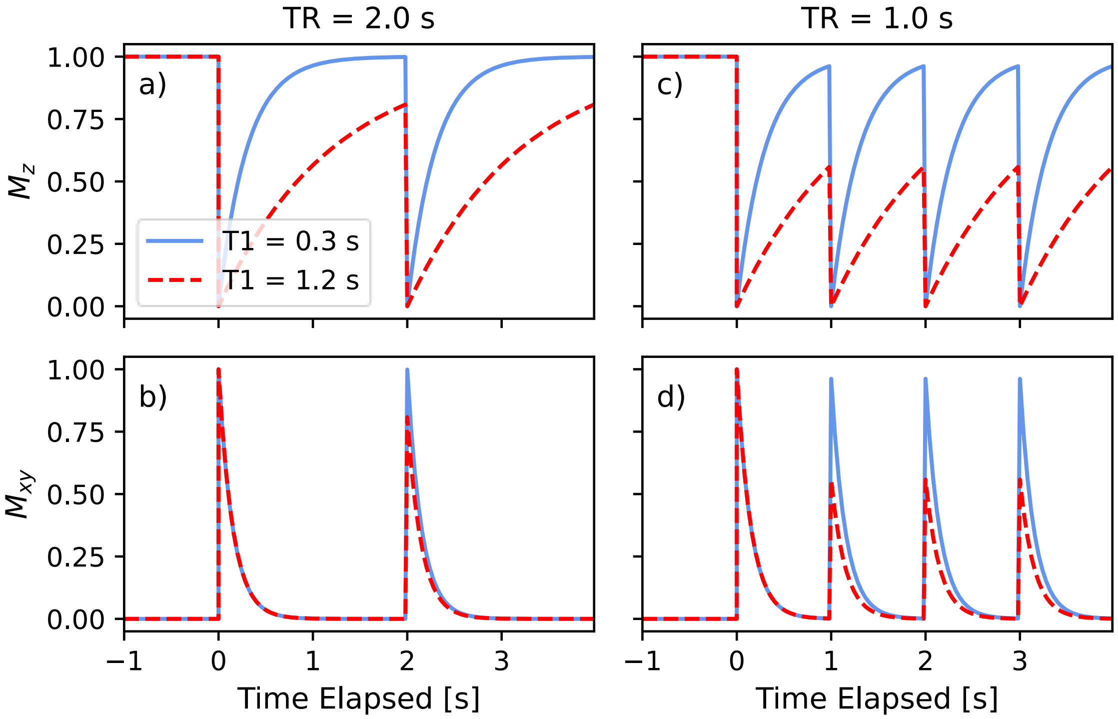

Figure 3: Effect of repetition time on the axial and transverse magnetization of materials with different axial relaxation rates. The transverse magnetization decays freely because there is no phase or frequency encoding in this example.

2.3.3 Flip Angle

A shorter TR allows for a shorter scan duration, but the accompanying T_1-weighting may be undesired. Reducing the FA leaves some longitudinal magnetization available for subsequent excitations and reduces T_1 contrast (Figure 4, top row). However, smaller FAs tip less transverse magnetization, resulting in lower signal (Figure 4d). In other words, combinations of FA and TR can be selected to fine-tune the contrast, with the consequence of affecting the overall signal.

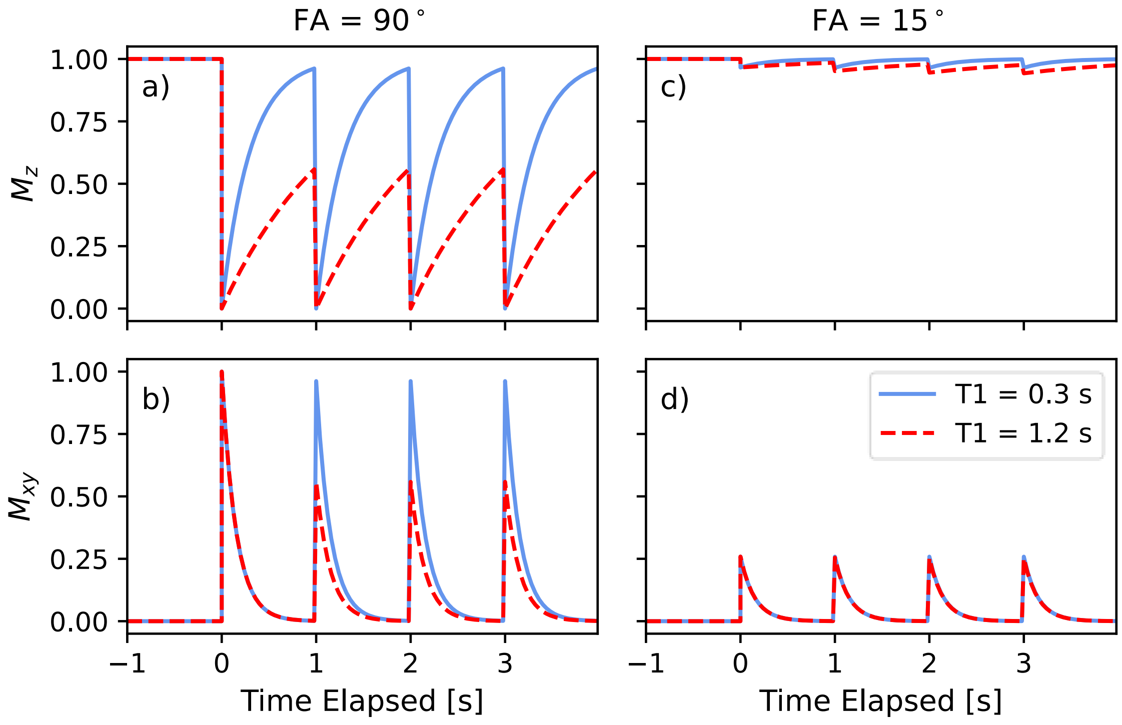

Figure 4: Effects of flip angle on the longitudinal and transverse magnetization of materials with different T_1. In this example, the transverse magnetization decays freely in the absence of phase or frequency encoding. A TR of one second is used in both scenarios.

2.4 Ultra-Short Echo Time Imaging

Ultra-short echo time (UTE) pulse sequences can produce images of tissues with very short transverse relaxation times, also called short T_2 tissues[15]. The signal from short T_2 tissues can decay too rapidly for detection, making them invisible on images. This is the case for cortical bone which features a T_2 of 0.39 ms in magnetic fields of 3 T[16]. For comparison, gray matter features a T_2 of approximately 100 ms[17]. To make bone visible on MR images, TE should be minimized, and the following signal should be measured as fast as possible following the excitation.

The minimum TE possible with sequences that use phase encoding pulses as described in section 2.2 is limited to 1-2 ms[18] because of limitations imposed on gradient fields for patient safety[19]. Sampling k-space from the centre out eliminates the need for phase encoding gradients. In this case, the limitation preventing a 0 ms TE is the time the scanner needs to switch from transmit to receive mode[20]. Most centric sampling schemes fall under one of two umbrellas: radial and spiral sampling.

Imaging short T_2 tissues is not just a matter of minimizing TE. Rapid acquisition of signals in the outer region of k-space (minimizing decay) is important to achieve good spatial resolution[18]. The time between the first measurement at the center of k-space and the last measurement at the edge is called the readout duration. Minimizing readout duration is important for both radial and spiral pulse sequences.

2.4.1 Radial Acquisitions

Radial trajectories are the simplest centric sampling methods. k-space is filled starting at the centre, moving radially outwards over the readout duration (Figure 5, centre)[18]. In 3D, radial acquisition can take the form of a stack-of-stars[21] or a koosh-ball[22]. The stack-of-stars requires a phase encoding gradient to encode the 3rd dimension, increasing the minimum echo time but offering flexible slice thickness. Koosh-ball sequences are constrained to isotropic voxels and matrix sizes but offer a shorter minimum TE than stack-of-stars sequences.

The main challenge in radial acquisitions is to sample the high-frequency contents of the k-space while maintaining short scan times. Achieving the large grid sizes necessary for high resolution imaging or large field-of-views (FOV) necessitate a large number of spokes to satisfy the Nyquist criterion[23]. In koosh-ball sequences, the number of spokes needed to fully sample k-space must be greater than $\pi {N_{grid}}^2$, where N_{grid} is the length of the sides of the array. For the stack-of-stars sequences, the Nyquist criterion is $\pi N_{grid} N_{slices}$, where N_{slices} is the number of slices in the volume.

2.4.2 Spiral Acquisitions

Using a spiral trajectory instead of radial spokes samples k-space more efficiently and can subsequently shortens the total scan time[23]. While a single spiral could sample the entirety of k-space, limitations on the rate-of-change and amplitude of the gradient fields would result in a long readout duration. To shorten the readout, the sampling is distributed over several interleaves, each completed in different repetitions (Figure 5)[24].

In 3D, spirals can be arranged in a stack-of-spiral or in cones[25]. Like for a stack-of-stars, stack-of-spirals sequences use a z-gradient to select a slice in the volume before x and y-gradients can be used to draw an interleaf[26]. Otherwise, spirals can be wrapped around cones of varying angle stacked into one-another[27].

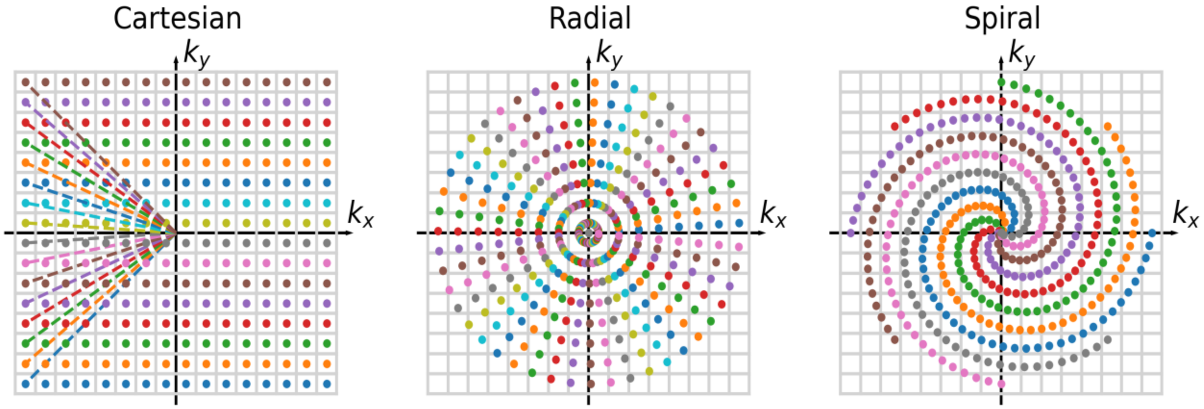

Figure 5: Different k-space trajectories. Points and dotted lines depict parts of trajectories described by readout and phase encoding gradients, respectively. Colours indicate the distinct interleaves, acquired over repetitions of these sequences. Center-out trajectories do not need phase encoding gradients.

2.4.3 Zero Echo Time Imaging

To further reduce the time elapsed from excitation to the sampling of an outmost point in k-space (TE + Readout duration), zero-echo time (ZTE) techniques can be used. While, our work does not rely on ZTE, many publications cited in this thesis do. This section, based on the review by Wiesinger *et al.*[28], summarizes this alternative approach to imaging short-T_2 tissues.

ZTE sequences are based on koosh-ball trajectories to minimize readout durations, but the gradients are never turned off. After a readout, a non-selective RF pulse is used as the gradients are adjusted slightly to select another spoke in k-space. With this strategy, no time is lost while gradients are ramped up and the receive coils are switched from transmission to reception mode. However, no signal can be acquired during the receive coils mode switch, leaving an unsampled hole at the center of k-space. ZTE approaches vary on the filling of this void: some acquire individual points using a UTE koosh-ball sequence that covers the hole, while others interpolate the center region of k-space if it is small enough.

2.5 Colour Image Segmentation

2.5.1 Colour Spaces

Colours are represented by a minimum of three components. Just like a vector can be represented using different basis vectors in linear algebra, colours can be represented using different colour spaces. This section, providing information on the colour spaces relevant to this project, is based on the textbook by Fernandez-Maloigne *et al*.[29]

The red-green-blue (RGB) colour space is used for digital media acquisition, storage, and display. The three channels store the intensity of red, green, and blue light detected by camera sensors or emitted by diodes in screen pixels. Although convenient for digital hardware, RGB space does not accurately represent how humans perceive colours. One of the biggest repercussions of this limitation in image segmentation is that Euclidean distances cannot be used to assess the similarity between pairs of colours.

The CIELAB colour space proposes a numerical representation of colours that corresponds to human perception, from a simple formula. The Euclidean distances in this space can approximate the perceived differences between colors. To recreate human perception, the CIELAB colour space is based on Ewald Hering's theory of opponent channels. According to this theory, the human brain interprets light based on three pairs of opposing colours: white and black, blue and yellow, and green and red. The CIELAB colour space uses lightness (L*), a*, and b* to represent these opposing pairs, respectively. Figure 6 illustrates the channels of the RGB and CIELAB spaces.

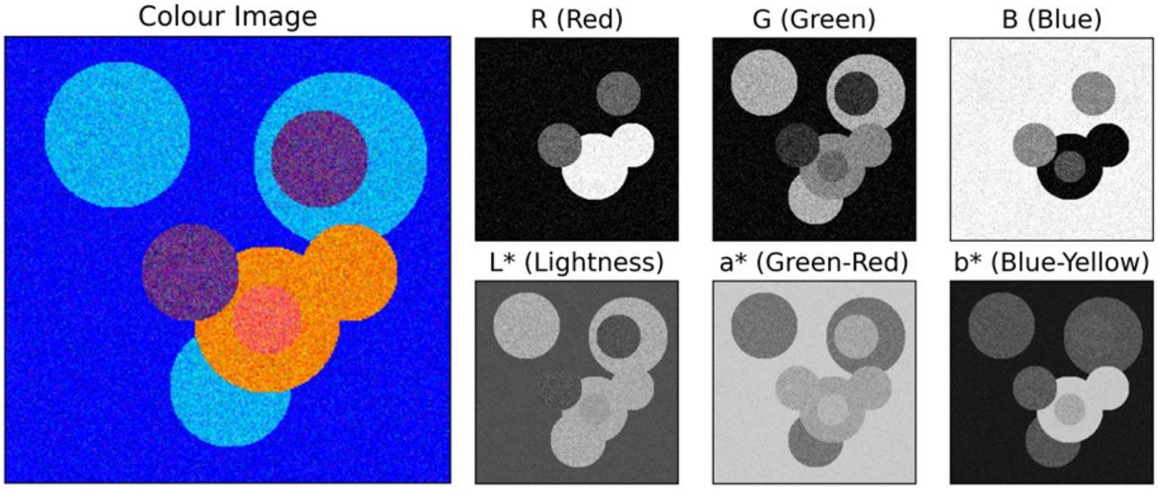

Figure 6: RGB (top row) and CIELAB (bottom row) channels of the image on the left.

2.5.2 Clustering

Clustering refers to the task of grouping data points with similar properties into different classes, called clusters. Similarity is defined differently depending on the clustering algorithm used[30].

K-means clustering is one of the simplest clustering algorithms[31]. The user defines the number of clusters, and the algorithm randomly assigns centroids in the domain of the data points. Each data point is assigned to the closest centroid using the type of distance the user wants, such as Euclidean or Manhattan for example. The positions of the centroids are recalculated as the centres of mass of each clusters. The point assignment and centroid calculations are iteratively repeated until the sum-of-squared distances within a cluster converges to a stable value.

Using centroids has the disadvantage of constraining the algorithm to be used on spheroidal clusters[32]. Figure 7 demonstrates the difference in performance of k-means clustering on globular and annular clusters.

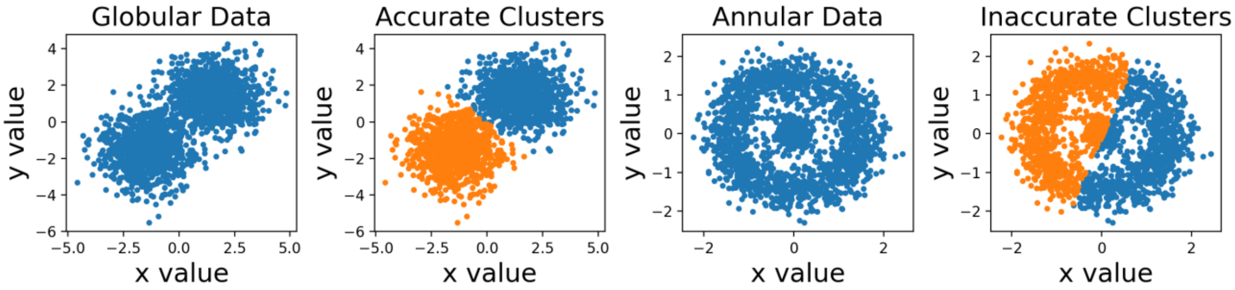

Figure 7: K-means clustering of globular and annular data.

Clustering can be used for colour image segmentation by representing pixels as data points using their colour parameters as coordinates[33]. Figure 8 depicts the segmentation of a noisy colour image using k-means clustering in both RGB and CIELAB colour spaces. Figure 9 also illustrates how segmentation benefits from Euclidean distances to represent perceived colour differences in CIELAB colour space.

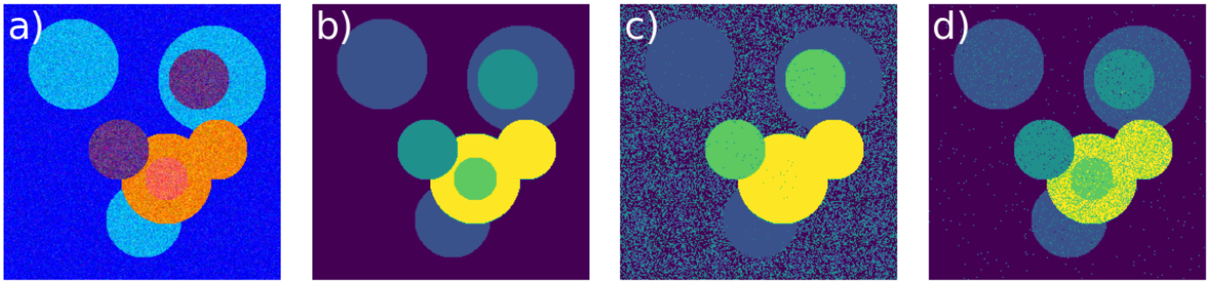

Figure 8: Segmentation of Figure A using K-means clustering. Original colour image (a), ground truth segmentation, where the new colours are labels for the five clusters (b), segmentation resulting from clustering in RGB space (c) and CIELAB space (d).

Fuzzy-C-means (FCM) clustering is a modified version of k-means clustering that allows for probabilities to be assigned to each data point[34]. Data points situated between two clusters can be described as a mixture of classes instead of being assigned a label based on the closest centroid.

2.5.3 Simple Linear Iterative Clustering

Images can be segmented using clustering methods (subsection 2.5.2). To increase the accuracy and robustness of the segmentation, the coordinates (x, y) of each pixel can be added as extra dimensions to the data points, to consider for the spatial proximity of pixels (i.e. using L*, a*, b*, x, y). This method only performs well over short distances if spatial coordinates are heavily weighted, or over longer distances if colour is weighted preferentially. With the method exclusively working at long or short distances, segmenting entire images cannot be achieved reliably. This section describes the simple linear iterative clustering (SLIC), a solution to the spatial weighting problem proposed by Achanta *et al.*[12]

The SLIC algorithm solves this problem by assessing the colour similarity of pixels in spatially restricted neighborhoods. SLIC begins by defining a user-specified number of regions which are used to constrain the k-means clustering of colours and spatial coordinates. The spatial components of the resulting clusters are then used as the centres of a new set of regions. The shapes of the new regions are also optimized to reduce their internal colour variance. The algorithm then iteratively repeats the process until the variance in colour within the regions is minimized (Figure 9). In the field of computer vision, the regions produced by SLIC and similar algorithms are called superpixels. They act as large irregularly shaped pixels in further segmentation steps.

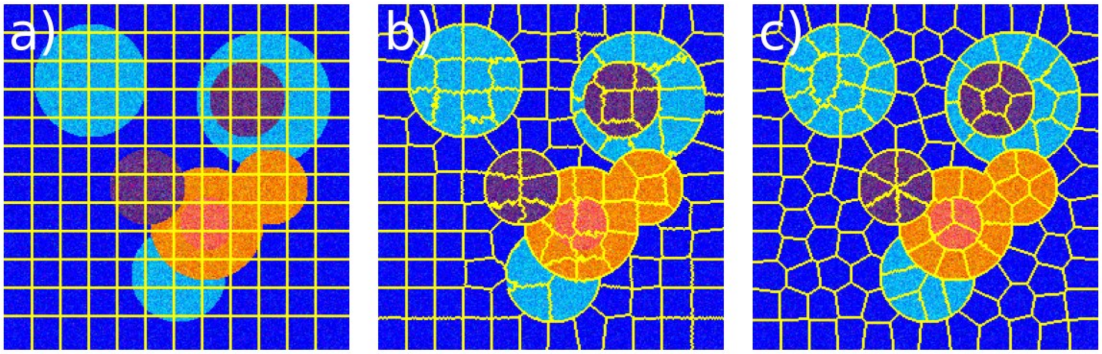

Figure 9: 1st , 3rd, and 30th iteration of the SLIC algorithm on a noisy colour image.

2.5.4 Region Adjacency Graphs

Superpixel algorithms are not used for complete segmentations because they often assign different labels to neighbouring regions of similar colour that need to be merged (for example, the lighter orange shape in Figure 9 is divided into 13 superpixels). This merging process can be achieved using a region adjacency graph (RAG)[35]. In this graph, each superpixel is a node and neighboring superpixels are connected using lines. Figure 10a depicts a RAG over an image processed using SLIC.

For every line, a dissimilarity metric can be computed, such as Euclidean distance in CIELAB colour space between the mean colour of the connected superpixels. Algorithms can then be used to determine which nodes can be merged. The simplest approach is to merge superpixels whose dissimilarity falls below a predefined threshold[13]. Figures 10b and 10c illustrate segmentation using an appropriate (b) and an overestimated (c) threshold, respectively.

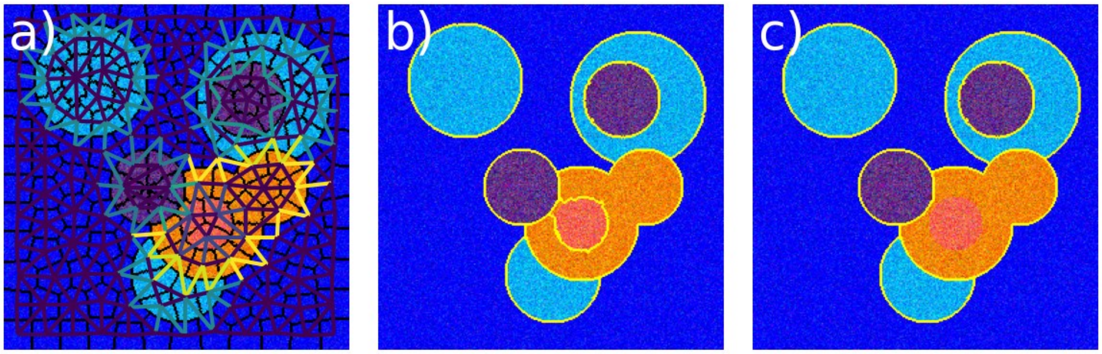

Figure 10: RGA thresholding of Figure 9c. RAG (a), Superpixels merged using an appropriate threshold (b), and an excessive threshold (c).

2.6 Computed Tomography in Radiotherapy Treatment Planning

2.6.1 Computed Tomography

Tomography describes the problem of reconstructing cross-sections of objects from multiple projection images acquired using penetrating waves. Computed Tomography (CT) refers to a medical imaging modality which uses kilovoltage X-ray projections of patients to produce images of their internal anatomy. For further information about CT image reconstruction techniques and hardware considerations, the reader is directed to the textbooks by Herman *et al.*[2] and Samei *et al.*[36] respectively.

Axial slices of the anatomy of patients are typically reconstructed with filtered back projections or iterative reconstruction methods. Reconstruction methods quantify the X-ray absorption properties of voxels and encodes them in the pixel values of the images, called CT numbers. These numbers are given in terms of Hounsfield units (HU), defined in equation 2.6.1.1, where μ and μ_{water} are the linear attenuation coefficients[1] of a given voxel and of water respectively.

$$\text{CT number} = 1000 \times \frac{\mu - \mu_{\text{water}}}{\mu_{\text{water}}}\ \text{HU} \qquad 2.6.1.1$$

CT scanners are calibrated for air and water to have CT numbers of -1000 HU and 0 HU respectively. Section 2.6.2 will expand on the use of CT numbers in radiotherapy.

2.6.2 Radiotherapy Treatment Planning and CT simulation

Radiotherapy aims at killing cancer cells using radiation while minimizing the dose to healthy tissues to reduce the severity of adverse effects. This section outlines the careful process of radiotherapy treatment planning (RTP) in external beam radiotherapy (EBRT), which is thoroughly discussed in the book by Barrett *et al*.[37]

In EBRT, beams of X-rays at megavoltage (MV) energies are produced by linear accelerators (linacs) and directed at the target from multiple angles to spread the entry dose and avoid organs at risk (OAR). The total dose of radiation is also delivered over multiple days (fractions). Determining the positioning of beams, and the quantity of radiation delivered at each position requires careful planning based on CT images.

The acquisition of CT images for the purpose of RTP is called CT-simulation because the positioning of the patient and the use of fixation devices and bolus are determined for the treatment during this phase of planning. The CT scanners dedicated to simulating treatments are often named CT-simulators. They usually feature external laser positioning systems reminiscent of the ones found in treatment rooms, wider bores to accommodate fixation devices, and flat couch surfaces to replicate the ones found on treatment units[38].

The images acquired on CT-simulators are first used to contour targets and OARs and to define the treatment isocentre. The visible lesion is defined as the gross tumour volume (GTV). To account for microscopic cancer cells that could surround the tumour, a margin around the GTV is added, resulting in the definition of the clinical target volume (CTV). To further account for treatment uncertainty, such as errors in position and patient motion, a second margin is added to the CTV, leading to the contouring of the planning target volume (PTV). RTP clinical coverage goals are usually defined for the PTV.

CT images are also used to compute the dose delivered by different beam configurations to optimize the treatment. Many algorithms have been developed to compute the dose to patients accounting for tissue heterogeneities, and rely on maps of electron density estimated from CT numbers[39]. Linear relationships between relative electron density (RED) and CT numbers have been established in the past[3].

Moreover, the position of patients is ascertained with the planning CT images before the delivery of their daily fraction. Modern linacs are equipped with kilovoltage X-ray tubes and flat panel detectors to acquire projection images of patients, an apparatus called on-board imaging. On-board imaging can be used to produce cone-beam CT (CBCT) images of the patients lying on the treatment couch. By comparing CBCT and planning CT, patient alignment can be validated[40].

2.7 Magnetic Resonance in Treatment Planning

MRI is routinely used alongside CT for treatment planning. Because soft tissues have similar atomic compositions and electron densities, CT provides limited soft-tissue contrast. In certain sites, like the brain, head and neck, and pelvis[41], MRI is necessary to adequately contour targets and organs at risk. Unfortunately, MR images cannot be used directly to estimate relative electron densities, so CT is still needed for dose calculations. To simultaneously use MR images for contouring and CT for dose calculation, both series of images need to be aligned in a process called registration.

2.7.1 Registration of MR with CT

The anatomy visible in MR images needs to share the same coordinates as in CT images to be used for contouring. In clinics, rigid registration is the most commonly used technique according to surveys[42]. In this method, MR images are aligned using translations and rotations in 3D, assuming that the anatomy is rigid. This process introduces errors in the treatment plan because MR-specific artifacts, geometrical distortions, and variations in patient anatomy between the two scans violates this assumption of rigidity. In brain plans, the spatial error on the targets position was reported to be 1.8 ± 2.2 mm[5]. A similar error of 1.9 mm was observed in prostate cases[43]. To ensure the adequate coverage of the CTV, greater margins must be included in the PTV, which implies that a greater volume of healthy tissue is irradiated.

2.7.2 MR-only Radiotherapy

Ending the use of CT-simulation in favor of an MR-only RTP workflow would eliminate the registration process and its accompanying error. Moreover, reducing the number of scans needed per patient lowers the workload and costs associated with treatment planning[44].

To enable dose calculations, great efforts have been made to generate synthetic CT (sCT) images using MRI[45,46]. Besides approximating RED, synthetic CT images can also be used to validate patient positioning on on-board imaging[47]. Outside of RTP, sCT could be used to compute photon attenuation maps for positron emission tomography (PET) to enable attenuation corrections in PET/MR systems[48-53].

Chapter 3: Review of CT Synthesis Algorithms

This chapter is dedicated to the review of numerous CT synthesis techniques that have been proposed in the past decade, including atlas-based methods, machine learning approaches, generative adversarial networks, commercially available neural networks, and deterministic methods. An overview of the importance of accurate bone segmentation will precede the review to inform the reader about the challenges of sCT. The state of the field of CT synthesis has also been assessed in multiple recent reviews[4,45,46,54,55].

In this chapter, the inner workings of some of these algorithms will be described in short summaries and their performance will be outlined, primarily by using the mean absolute error (MAE) between sCT and X-ray CT numbers and the scan time necessary to acquire input data that is not part of the normally acquired planning images. Groups researching sCT usually recompute the dose from existing treatment plans on sCT images and compare it to the dose initially obtained on X-ray CT using Gamma analysis, which is explained elsewhere[56]. While the work in this thesis did not reach this step of validation, dose accuracy of select methods will be highlighted in Table 1, which summarizes the selected methods discussed in this chapter. Recent publications usually report Gamma pass rates of above 99% for the 3% / 3 mm criterion[46,54].

3.1 On the Importance of Bone in CT Synthesis

Due to its rapid transverse relaxation and low proton density, cortical bone is generally invisible on MR images, and is indistinguishable from air[57]. Except for metal implants, bone absorbs the most radiation in the human body whereas air has negligible effect on the transmission of radiation[58]. Thus, on CT, air and bone exhibit the greatest naturally-occuring contrast difference.

From an RTP perspective, the correct representation of air and bone has significant impact on the accuracy of the dose prediction[59,60].

Moreover, contrary to other tissues, bone (cortical and trabecular) has a wide range of CT numbers, usually between 200 HU[61] to 2000 HU[62]. Given that errors of 100 HU result in a deviation of 2% on calculated PTV dose[63], we can infer that assigning uniform sCT numbers to all bone structures would result in significant errors on RTP dose calculations. For accurate CT synthesis, bone density information should be extracted from the MR images for sCT numbers to be estimated in bones.

3.2 Atlas-based Techniques

In atlas-based methods, the CT and MR images of previous patients are registered and saved in pairs in a database referred to as an atlas. For a new patient for whom an sCT image must be produced, the MR images of the atlas are transformed using deformable registration to match the new MRI scan. The transformation applied to the MR images of atlas are also used on the paired CT images[64]. In most atlas-based approaches, registration errors in a given voxel are calculated for the corresponding voxels in each MR image of the atlas[64-69]. The sCT number of this voxel is computed using a weighted average of CT numbers of corresponding voxels in the CT images of the atlas, where the weighting is the registration error. This approach has been explored in the pelvis[70], brain[71], and head and neck[72].

Generally, better results were obtained with atlas methods in the pelvis (MAE of around 40 HU)[66,72,73] than in the head (MAE over 150 HU)[69,71]. Dowling *et al.* developed an atlas-based sCT algorithm from 39 prostate cases and reported an average Dice similarity coefficient (DSC) of 0.79 for bone[70]. Using an improved version of the same algorithm, Wyatt *et al.* reported an improved DSC of 0.95 for bone across two main magnetic field strengths (1.5 T and 3 T)[74]. No mean absolute errors (MAE) where reported in these publications. However, in another atlas-based sCT algorithm tailored for prostate cancer, Farjam *et al.* used the images of 23 patients to obtain an average MAE of 47 ± 5 HU for entire images and 116 ± 12 HU for bony anatomy[75].

To increase the accuracy of atlas-based methods for brain cases, Demol *et al.* proposed a modified atlas-based method that assigned sCT numbers on voxels based on a search of neighboring voxels with similar MR signal instead of using spatially corresponding voxels. Although this method produced sCT images with more plausible appearances, it introduced a significant amount of blurring. Demol *et al.* reported an average MAE of 150 HU for the whole volume, and 650 HU for bone specifically.

3.3 Machine Learning

In parallel to developments in atlas-based methods, other groups focused on early machine learning approaches, such as Gaussian mixture regressions[76] and random forests[77,78]. Instead of averaging images from a database, machine learning approaches are built on the hypothesis that such databases can be used to determine relationships between MRI signal intensity and CT numbers. This way, the relationship between the voxel intensities of the two modalities could be used to directly calculate an sCT image from MRI. Machine learning approaches predating the widespread use of neural networks are scarce but have been investigated for brain[79,80] and prostate[80,81] cases.

Johansson *et al.* acquired five MR images from five patients with brain cancer: two dual-echo UTE sequences with different flip angles, and a T_2-weighted (T2w) spin echo sequence. For each of these five images, two additional images were constructed from the mean and standard deviation (STD) of the 27-voxel neighbourhood of every voxel. Hence, every voxel was represented by 16 signals: five MR signals, five MRI local means, five MRI local STD, and a CT number. A Gaussian mixture regression model was trained on the combination of MR and CT images to effectively fit 20 multivariate Gaussians to a 16-variable function[79]. This method was tested using a leave-one-out scheme[82], training the model on four patients and testing on the last subject. The process was repeated such that data from all patients were used for testing. The MAE of sCT images computed from the fit parameters averaged 137 HU, ranging from 117 HU to 176 HU[79].

As for atlas-based methods, early machine learning methods performed better in images of the pelvis. Largent *et al.* used a random forest model trained on 96 manually chosen features such as edge information and texture metrics. Their method achieved an MAE of 45.79 ± 10.02 HU across their cohort of 10 patients diagnosed with prostate cancer, using a leave-one-out scheme for testing. They noted that this result was worse than what would be obtained with an atlas-based method on the same cohort[81].

3.4 Generative Adversarial Networks

Advancements in machine learning – more specifically deep learning – led to the development of neural networks which can define features without human intervention, eliminating the need to manually determine which features in the data should be fitted by the model[55,83]. Generative adversarial networks (GAN) are a particular type of neural network which has been popular for CT synthesis in recent years[45,46,55]. GANs use two different neural networks: a generator and a discriminator[84]. During training, the generator produces sCT images from MRI while the discriminator assesses if they are X-ray or synthetic CT images given the input MRI data. Over multiple iterations of training, the generator improves the quality of the sCT to trick the discriminator while the latter improves its authentication of the output images.

Most newly proposed methods rely on variations of GAN and numerous literature reviews focusing entirely on these networks have been written in different medical fields[46,49,85,86]. The use of GAN was explored in the brain[87,88], breast[89,90], head and neck[91,92], liver[93], pelvis[94,95], abdomen[96,97], thorax[98], and rectum[99]. Across these different sites, average MAEs reported since 2022 ranged from 26 HU to 93 HU, with the best performances observed in prostate cases, and the worst in the head and neck. Head-and-neck is a difficult area to scan due to breathing and swallowing motion, variations in cross-sectional diameter which introduce magnetic field inhomogeneities, and various challenges in coil design[100].

A typical use of GAN for CT synthesis consists in training a network on pairs of registered CT and MR images from cancer patients. For example, Tang *et al.* trained a GAN to translate T1-weighted (T1w) turbo inversion recovery dark fluid spin echo images to sCT on a cohort of 27 patients with brain cancer. They obtained a MAE 60.52 ± 13.32 HU on a testing dataset of 10 patients[101].

To obtain a more generalized algorithm, Jabbarpour *et al.* trained their GAN with a variety of T_1 and T2w images, from spin echo or gradient echo sequences, even featuring non-cartesian acquisitions like periodically rotated overlapping parallel lines with enhanced reconstruction (PROPELLER). When trained on a cohort of 150 patients and tested on 39 other patients, the resulting sCT images achieved a MAE of 80.11 ± 29.10 HU for T1w inputs, and 75.00 ± 20.00 HU for T2w[102].

So far, all methods presented in sections 3.1 to 3.4 required MR images to be registered to their counterpart X-ray CT images. Even conventional GANs cannot be trained on unpaired images[84], thus limiting the practical size of the training dataset. Sun *et al.* investigated cycle-consistent GANs[103] (cycleGAN) to overcome this limitation. In this architecture, two GANs sharing the same generators and discriminators are arranged in a ring-shaped pipeline and constrained by a cyclic loss function enabling them to efficiently learn the non-linear mapping between two different image domains[84]. Training a cycleGAN model on unpaired T1w MR and CT images of 80 cervical cancer patients (increased to 120 through translations and rotations) yielded sCT images with an average MAE of 46.79 ± 2.76 HU[104].

3.5 Commercially Available Neural Networks

Three commercially available CT synthesis software solutions were identified in this literature review, sold by Spectronic Medical AB, Siemens Healthineers, and Philips Healthcare, respectively. These proprietary algorithms rely on neural networks and have been validated for brain cases by a handful of research groups as follows.

MRI Planner (Spectronic Medical AB, Helsingborg, Sweden) uses a convolutional neural network which requires 3D IDEAL Dixon images[105] that can be acquired in 4.5 minutes. Using the brain scans of 20 patients, Lerner *et al.* reported an MAE of 62.2 ± 4.1 HU using *MRI Planner*, ranging from 56.2 HU to 70.4 HU when fixation devices were excluded from the CT number comparison. The authors also noted that the algorithm performed marginally worse in patients with resected bone, following surgery. In their cohort, the images of 14 patients who underwent craniotomy had an MAE of 176.5 ± 18.8 HU for bones of the skull, compared to an MAE of 164.1 ± 14.4 HU for the 6 patients that were not operated[106].

Syngo.via VB60 RT pro edition (Siemens Healthineers, Erlangen, Germany) can synthesize CT images from pre-contrast T1w in-phase and opposed-phase images using two neural networks instead of relying on a GAN or a cycleGAN. The first network segments images while the second assigns continuous sCT numbers to the different tissues. Using data from 25 patients with brain cancer, Masitho *et al.* concluded that the sCT images had an MAE of 135.8 ± 12.9 HU, excluding fixation devices, and that craniotomy observed in nine of the 25 patients had a negligible effect on the accuracy of the algorithm[47].

The convolutional neural network of *MRCAT* (Philips, Vantaa, Finland) can be used to produce sCT scans from T1w multi-point Dixon (mDixon) images normally acquired in 2 minutes and 56 seconds. In a study by Ranta *et al.*, sCT images derived from brain scans of patients had an MAE of 63 HU, ranging from 50 HU – 82 HU in 50 patients with gliomas or metastases[107].

3.6 Deterministic Methods

Closer to the method proposed in this thesis, deterministic algorithms (or voxel-based methods) do not rely on any databases, but rather on voxel intensities of one or more MR images to assign sCT numbers[4]. Since these methods do not require any training, they are believed to be easier to adapt to different parts of the body or to patients with atypical anatomy[4,108]. These algorithms can rely on UTE or ZTE imaging for bone visualization[50,53], fat-water separation for soft tissue characterization[108,109], and FCM clustering for segmentation[110,111]. Deterministic algorithms have been developed for the brain[48,50,51], the head[10,52,53], the head and neck[10,110], the liver[111], the thorax[108,109], and the pelvis[112], showing good performance with average MAE ranging from 50 HU to 150 HU.

In one method based on a single proton density-weighted (PDw) ZTE image acquired in 2 minutes 51 seconds, Wiesinger *et al.* segmented air, soft tissue and bone using thresholds[53]. While homogeneous sCT numbers were assigned to air and soft tissue, bone regions were assigned sCT numbers based on a known negative linear relationship between PDw MR signal and CT numbers[113]. In the algorithm proposed by Wiesinger *et al.*, partial volume voxels mixing air and soft tissue, which can have the same intensity as bone, were segmented based on the intensity of neighboring voxels and assigned values based on the PDw signal. This algorithm produced sCT images with an average MAE of 123 ± 25 HU over scans of whole heads including the upper neck[53].

Some deterministic methods require multiple MR images of different contrast as inputs. For instance, Su *et al.* developed a CT synthesis method for imaging lungs based on the clustering of fat and water images acquired with a free breathing UTE mDixon protocol usually lasting 4 minutes 44 seconds[108]. To validate this method, 25 healthy volunteers were scanned. Their anatomies were used to create numerical 4D phantoms using the XCAT toolbox[114] to simulate CT scans. The bones in the simulated CT images of the phantoms were replaced with bones from acquired CT images of patients through deformable registration to recreate the greater variability of CT numbers present in bony anatomy. The sCT images generated from the real MR images of the volunteers were quantitatively compared with the simulated CT scans. This group reported an MAE of 50 HU for whole volumes and 100 HU for bone alone[108].

Approaching the bone-air differentiation problem from another angle, Fortier *et al.* proposed an algorithm relying on magnetic susceptibility to identify bone[10]. In their method, a single multi-echo acquisition was used to obtain a quantitative susceptibility map, fat and water images, and quantitative fat and water maps. These images were used for segmentation and to calculate sCT numbers based on probabilities derived from FCM clustering. They tested their method in a cohort of patients treated for cancers of the brain and of the head and neck, reporting MAEs of 105 HU and 112 HU, respectively.

Author	Year	Method	Site	MAE [HU]	Γ (3%/3 mm)	Γ (2%/2 mm)	Γ (1%/1 mm)
Dowling *et al.*[70]	2012	Atlas-based	Prostate	47 ± 5	N/A	N/A	N/A
Wyatt *et al.*[74]	2017	Atlas-based	Prostate	N/A	N/A	98.8±0.5	N/A
Farjam *et al.*[75]	2018	Atlas-based	Prostate	N/A	97.9	97.1	92.7
Johansson *et al.*[79]	2011	Gaussian Mixture	Brain	137	N/A	N/A	N/A
Largent *et al.*[81]	2017	Random Forest	Prostate	45.8 ± 10.0	N/A	N/A	99.2
Tang *et al.*[101]	2021	GAN	Brain	60.5 ± 13.3	N/A	99.8	97.2
Jabbarpour *et al.*[102]	2022	GAN	Brain	80.1 ± 29.1	99.0±1.1	95.0±3.7	90.1±6.0
Sun *et al.*[104]	2022	CycleGAN	Cervix	46.8 ± 2.8	N/A	95.4±1.9	N/A
Lerner *et al.*[106]	2021	*MRI Planner*	Brain	62.2 ± 4.1	100.0±0.0	99.8±0.2	99.1±0.6
Masitho *et al.*[47]	2022	*Syngo.via*	Brain	135.8 ± 12.9	N/A	N/A	N/A
Ranta *et al.*[107]	2023	*MRCAT*	Brain	63	N/A	98.0±2.1	82.1±7.6
Wiesinger *et al.*[53]	2018	ZTE image threshold	Brain	123 ± 25	99.9 ± 0.1	99.6±0.5	98.7±1.0
Su *et al.*[108]	2019	mDixon image clustering	Lungs	50	N/A	N/A	N/A
Fortier *et al.*[10]	2021	Susceptibility mapping	Brain / ENT	105/112	N/A	N/A	N/A

Table 1: Summary of selected methods discussed in this review of synthetic CT, comparing the type of method, the site of application, the reported mean absolute error (MAE), and the gamma pass rate in cases where dosimetric calculations were performed.

Chapter 4: Synthetic Computed Tomography from Colour Segmentation of Magnetic Resonance Images

Preface:

This chapter presents a manuscript that will be submitted to *Physica Medica*: European Journal of Medical Physics. This work describes our novel approach to CT synthesis, beginning with a justification of the work. Then, the methods by which images were acquired on MRI are described followed by a description of the sCT algorithm. Afterwards, the experimental protocol used to quantify the accuracy of this method in a phantom and qualitatively evaluate it in images of human heads are explained. Subsequently, the results of these tests are presented. Finally, these results are discussed as well as some limitations of the algorithm.

Title: Synthetic Computed Tomography from Colour Segmentation of Magnetic Resonance Images

Authors: Jules Faucher[1], Evan McNabb[2], Véronique Fortier[2,3], Ives R. Levesque[1]

[1]Medical Physics Unit, McGill University,

1001 boulevard Décarie, Montréal, Québec, Canada, H4A 3J1

[2]Medical Imaging, McGill University Health Center,

1001 boulevard Décarie, Montréal, Québec, Canada, H4A 3J1

[3]Department of Radiology, McGill University,

1650 Cedar Avenue, Montréal, Québec, Canada, H3G 1A4

Corresponding Author: Ives R. Levesque, ives.levesque@mcgill.ca

Highlights:

- Colour images created from multiple magnetic resonance images with different contrast can highlight different tissue types
- Deterministic color image segmentation methods can be used to differentiate tissue types on these colour images to create synthetic CT images.
- The proposed algorithm has the potential to adapt to different geometries and anatomies.

Funding: This work was supported by a *Bourses de maîtrise en recherche* scholarship from the Fonds de Recherche Nature et Technologies du Québec [grant number 334887], an *Établissement de jeune chercheur* award from the Fonds de Recherche en Santé du Québec, a Discovery Grant of the Natural Sciences and Engineering Research Council of Canada (NSERC), and the Montreal General Hospital Foundation.

Abstract

Purpose

To produce synthetic CT (sCT) images by using well-established colour-image segmentation techniques on red-green-blue (RGB) images created from multiple magnetic resonance (MR) scans.

Methods

In this technique, three spiral MR scans are acquired: ultra-short echo time (UTE) proton density-weighted (PDw) images, a UTE acquisition using the Ernst angle of bone for maximum bone signal, and a second echo of this bone-optimized sequence. These three sets of images are used as colour channels in an RGB volume. Voxels are merged into supervoxels using the simple linear iterative clustering algorithm, which are then classified based on their colour. Air, fat and soft tissue voxels are assigned bulk CT numbers, while bone voxels are assigned CT numbers calculated from the pixel values in the PDw images using a linear model (scale + shift). This method was tested quantitatively in a phantom featuring pieces of bovine femur, and qualitatively in human heads *in vivo*.

Results

Overall, the algorithm produced images with plausible appearance and differentiated between bone and air, with exceptions arising in voxels that were mixtures of air and soft tissue. In the phantom, the algorithm produced sCT images with a mean absolute error of 46 HU, and 222 HU specifically in bone regions. *In vivo*, details such as the mastoid air cells and turbinates were well represented. Some fat voxels were misidentified as bone.

Conclusion

The algorithm can synthesize CT images of phantoms and head images, with other anatomical sites still requiring investigation. Further optimization of the contrast of the input images could improve fat segmentation.

1. Introduction

In standard radiotherapy treatment planning (RTP), computed tomography (CT) images are needed for dose calculations but sometimes lack the soft-tissue contrast necessary for the accurate contouring of targets and organs-at-risk[1]. In these cases, additional magnetic resonance imaging (MRI) is needed for its superior soft-tissue contrast, and the images are registered to the CT images[2], still used for dose calculations since electron densities can be approximated from them[3]. Unfortunately, registration can introduce errors in the treatment plan[4,5]. Moreover, simulating the treatment on two different scanners takes a substantial amount of time, thus burdening the healthcare system[6]. For these reasons, there has been increasing interest in generating synthetic CT (sCT) images from MR images, allowing the patient to be scanned only using MRI for both contouring and dose calculation, thus simplifying the clinical workflow in RTP[1,7].

Multiple approaches for CT synthesis have been developed to address this need based on deterministic classification of tissues[8-10], atlas registration[11-13], or the training of an artificial intelligence (AI) model[14-16]. Regardless of the method used, the differentiation of air and bone remains the greatest priority, and challenge. Ignoring the potential presence of metal implants, cortical bone is the highest absorber of radiation in the human body[17]. Thus, bony anatomy has the greatest influence in the dose distribution in RTP. However, on typical clinical MR images, bone is invisible like air[18]. Hence, sCT methods need the capacity to differentiate bone from air on MRI. Deterministic algorithms typically need to acquire more data via extra sequences to gather information about bone structures, be it by detecting bone signal directly using ultra-short echo time (UTE) [19] or zero echo time imaging (ZTE) [8], or by detecting the effect bone has on the surrounding magnetic field with quantitative susceptibility mapping with iterative phase replacement[10]. Atlas-based methods eliminate the need for air-bone differentiation by relying on large databases of pre-registered MR and CT images of multiple of patients[11]. For a given patient's clinical images, the algorithm applies a deformable registration to the database images so that it matches the input, applies the same registration to the CT images in the database, and returns the transformed CTs as a weighted sum. AI-based methods also rely on large databases to train models that can compute sCT images from the input clinical MR images[7].

While sCT algorithms based on neural networks have been shown to accurately generate sCT images across multiple sites, deterministic methods are believed to be more robust in cases where patients have undergone extensive surgery or have atypical anatomies[1,9,20]. Unfortunately, deterministic methods that do not use any assumptions about the geometry of patients typically necessitate multiple MR acquisitions in addition to the clinical images, leading to substantial scan times[9,10,21]. Hence, there is still a need for a deterministic method that can operate with no geometrical assumptions and that exploits images acquired in a handful of minutes.

This work presents a new method for CT synthesis which does not exploit *a priori* knowledge or assumptions, and only needs an additional 4 minutes 14 seconds of scan time in the head to acquire the necessary input images. This novel technique is based on the segmentation of colours in RGB images created from three MR images to differentiate between the tissue types of importance in CT, those being water-based soft tissues, fat, bone, and air. This segmentation is used to assign Hounsfield units (HU) to the sCT. The following sections will describe our CT synthesis algorithm, from the MR acquisitions to the assignment of CT numbers, and the methods used to evaluate its performance both in a phantom and in the heads of volunteers. Finally, following a presentation of the results, the performance of the method will be discussed.

2. Methods and Materials

In the proposed method, three MR images with different contrasts are used as the colour channels of an RGB image. By using UTE imaging for some colour channels, this composite image contains information about bony structures. In the RGB image, each tissue class relevant to CT number assignment is depicted with different colours. Hence, tissues can be segmented based on their colour through well established colour image segmentation methods. The segmentation results are used to assign sCT numbers. Our methods were tested and optimized in a phantom and three volunteers.

2.1 UTE Acquisition

The MR images were acquired on a 3T system (Prisma, Siemens Healthineers, software version E11) using a non-selective stack-of-spirals UTE protocol (Siemens WIP992) and reconstructed using SPIRiT reconstruction[22] with a spiral iPAT factor of 2.

Three series of images were acquired. The first was a PDw UTE image to be used in both the RGB image and for CT number assignment of bone. Second, a “bone-optimized” image was acquired using the same parameters as for the PDw image but using an excitation pulse generating the Ernst flip angle of bone to maximize its signal. Finally, a second echo was collected with the bone-optimized sequence to act has a general T1-weighted image with negligible bone signal. The scan parameters for the UTE sequences are presented in Table 1. Sample images obtained with these parameters are shown in Figure 1.

In the initial experiments using the phantom, a clinically available magnetization prepared rapid gradient echo (MPRAGE) sequence was used to acquire a conventional T1-weighted image. This was used in the place of the second echo of the bone optimized image, as input to the segmentation. In this case the default acquisition parameters, optimized for brain imaging, were used: TR = 2300 ms, TE = 2.28 ms, TI = 900 ms, and FA = 8 degrees.

Through trial-and-error experimentation, the protocols were optimized, and parameters were modified. The TR was increased from 6 ms in the phantom experiment to 10 ms *in vivo* to increase the PD weighting of the PDw image. To compensate for the longer TR, the flip angle of the bone-optimized sequence was increased to 17 degrees. To shorten the scan time, the readout of the spirals was increased to 1.240 ms to reduce the number of spiral interleaves required to fulfill the Nyquist criterion, thus reducing the number of phase encoding steps needed.

Following the acquisition, an N4ITK bias-field correction[23] was applied to all MR images to improve their uniformity.

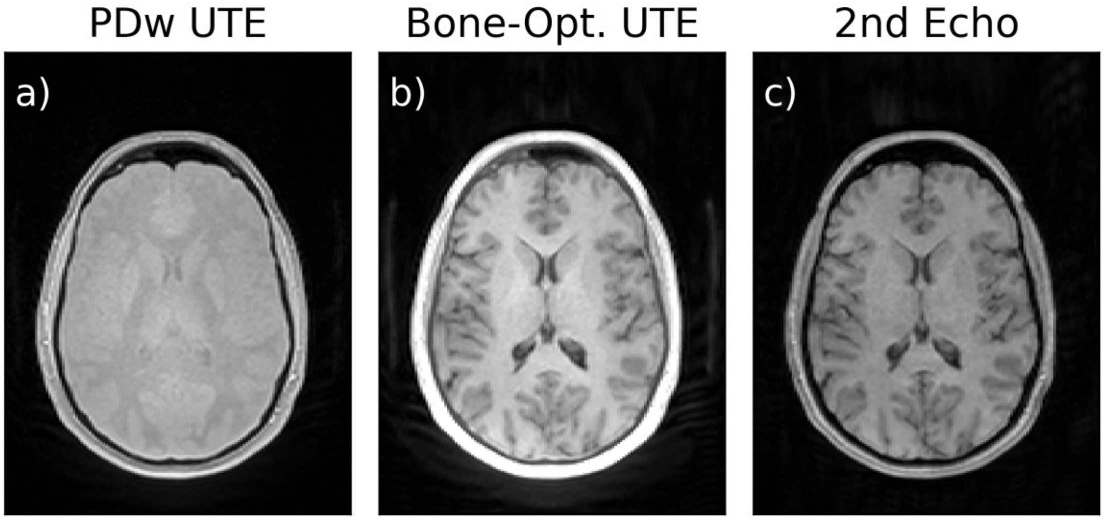

Figure 1: Input images acquired using the spiral ultra-short echo time (UTE) sequence. This figure displays examples of a) a proton density-weighted (PDw) image, b) the UTE-echo of a bone-optimized image and c) the second echo of the bone-optimized image, in an axial slice of a brain.

2.2 Image Segmentation and CT Synthesis

The CT synthesis algorithm was implemented in Python to follow the steps illustrated in Figure 2. The PDw UTE, bone-optimized UTE image, and the second echo of the bone-optimized acquisition were assigned to the green, blue, and red channel of an RGB image respectively. This order was chosen to reduce eye strain. The segmentation of the colour MRI image, to generate masks of the materials in the phantom or tissues in the human head, was performed in three steps: first, using the simple linear clustering (SLIC) algorithm[24], second, merging neighbouring SLIC labels of similar colours, and third, applying fuzzy C-means (FCM) clustering[25] to the merged labels.

In the first segmentation step, the SLIC algorithm divides the image into regions of spatially close pixels of similar colour which are refer to as superpixels, or supervoxels in 3D. SLIC first converts the RGB image into the CIELAB colour space since it better represents human perception of colour[26], thus yielding more accurate segmentations[27]. The various segmentation labels returned by SLIC were then assigned the mean value of the voxels contained within the label in the original RGB image to create a new, simplified image. A region adjacency graph (RAG) was then created to represent the colour similarity between neighboring supervoxels[28]. This similarity was defined as the Euclidean distance between the colours in CIELAB space. Neighbouring supervoxels whose colour similarity fell below the median of all similarities were merged to further reduce the number of regions in the image.

Following the application of SLIC, the colours in the superpixel image were clustered into six groups using the FCM algorithm, with initial guesses representing the colours expected from the six main materials observed in the head. These materials were air, fat, cerebrospinal fluid (CSF), water-based soft tissues (referred to as soft tissue in the rest of this work), mixtures of air and soft tissue (partial volume voxels), and bone.

After segmentation, the resulting binary masks representing each material were used to assign CT numbers, yielding the sCT. For air, fat, CSF, and soft tissue, bulk values of -1000 HU, -70 HU, 0 HU, and 40 HU were assigned, respectively. Partial volume voxels and bone voxels were assigned CT numbers based on their pixel values in the PDw image. For partial volume voxels, CT numbers were assumed to scale linearly with proton density, and thus with the PDw UTE signal intensity. For bone, there exists a negative linear relationship between PDw UTE signal and CT numbers in bone measurements[8,29]. A similar equation, calibrated using our phantom measurements, was used to compute bone CT numbers.

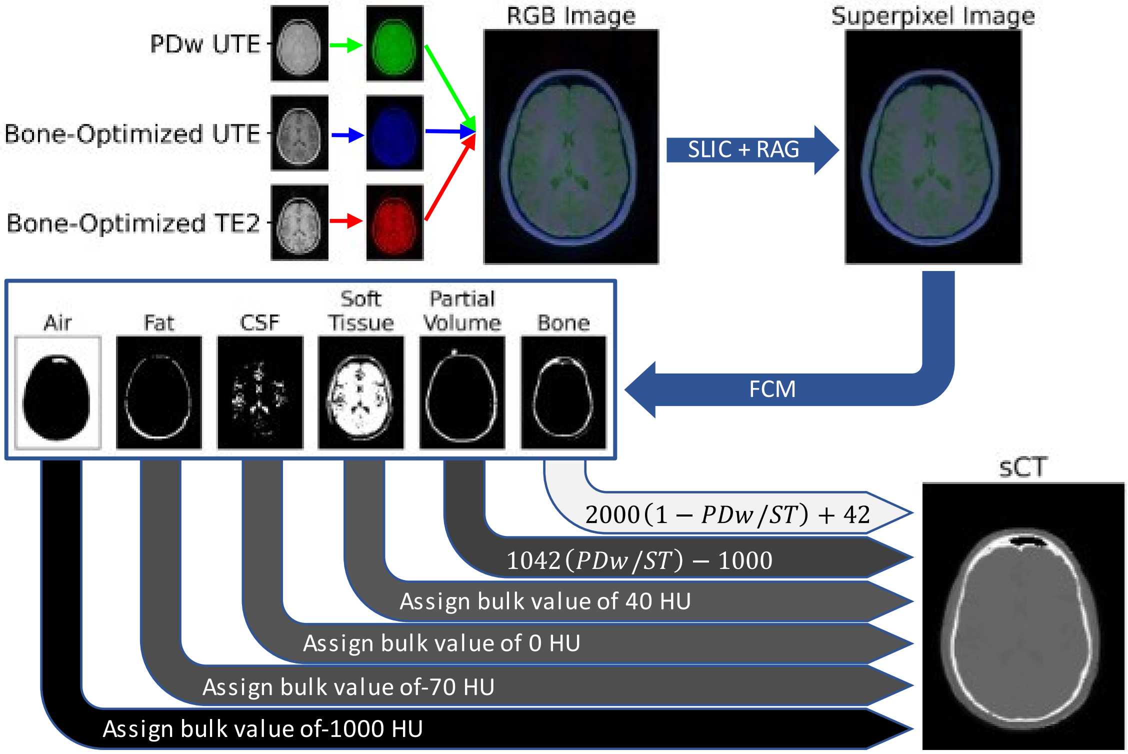

Figure 2: Flowchart representation of the CT synthesis algorithm. This figure illustrates how the three input images are combined into an RGB image to be segmented into different masks in a two-step process using SLIC and FCM (top). The masks are then used for CT number assignment to generate the final sCT (bottom).

To achieve sCT of the head instead of the phantom, the number of clusters used in the FCM was increased by one to segment CSF. The sCT numbers assigned to soft tissue (agar in the case of the phantom) was also increased from 13 HU to 40 HU.

2.3 Phantom Experiments

The phantom consisted of water-based gel in which various objects of interest were placed. The gel was a solution 1% agar (by weight) in of distilled water, with the addition of 0.5% table salt by weight to increase the conductivity of the phantom to ensure adequate B_1 homogeneity[30] and

0.05% sodium benzoate by weight, a common food preservative used to increase the lifespan of the gel. The solution was prepared in a beaker heated at 80 °C[31].

A first layer of gel was poured into a plastic container (Rubbermaid®) and cooled down in a refrigerator. Once the gel had set, the objects were placed on this layer: a fresh piece of bovine femur, a ping pong ball, a processed piece of bovine femur, and a piece of polyoxymethylene (Delrin®). Prior to placement, the fresh piece of bovine femur was kept frozen at -80 °C to prevent marrow from warming up and melting when the second layer of agar would be poured. The ping pong ball was added to create an air cavity. The second (processed) piece of bovine femur was manually emptied of marrow, cleaned with a brush and a caustic soda-based cleaning product, then soaked in distilled water for 10 days for rehydration[32]. Before being placed in the phantom, the second piece of femur was sealed at both ends using epoxy resin to create an air cavity adjacent to bone, mimicking the human sinuses. Finally, the piece of Delrin® was included to assess if plastic was visible with our UTE sequence. Delrin® in particular was selected for the small size of the magnetic susceptibility artifacts it generates[33]. The objects were covered in a second layer of agar, and the phantom was left in the refrigerator to solidify until it was scanned the next day.

X-ray CT images of the phantom were acquired on a CT-simulator (Brilliance Big Bore, Philips Healthcare) at a tube potential of 120 kVp. The highest dose allowed by the thermal limits of the X-ray tube was used (284 mA, 1002 mAs, $CTDI_{vol}$ = 119 mGy), to achieve the maximum signal-to-noise ratio and the most accurate CT number measurements for this reference scan. The images were reconstructed using a bone kernel and registered to the MR images acquired later. MR images were then produced the same day as described in the "phantom" column of Table 1.

Quantitative metrics were computed to compare the sCT to the X-ray CT in terms of CT number assignment and the underlying segmentation. To do so, the DICOM-format X-ray CT and MR images were imported into Python, where sCT images were generated. To quantify the accuracy into different materials, the CT images were segmented into masks representing bone, air, and the combination of agar and fat using thresholds. The bone mask was defined as pixels above 200 HU. The piece of plastic was included in the bone mask using this threshold, and it was manually removed. The air mask was defined as every pixel below -950 HU. The agar and fat mask were defined as all pixels between -950 HU and 200 HU. Partial volume voxels between air and bone regions had CT numbers in the same range as agar and fat, so they were manually excluded from the agar and fat mask. Using the X-ray CT images as ground truth, the mean error (ME), mean absolute error (MAE), and the intraclass correlation coefficient (ICC) were computed for the entire 3D volume, for bony structures, regions of air, agar, and fat.

To assess the quality of the segmentation, the masks used in the sCT algorithm were compared with CT-based segmentation described above to calculate the sensitivity, the specificity, and Dice's similarity coefficient (DSC) for bone, air, and agar and fat.

2.4 In Vivo Experiments

Following the approval of the research ethics board of the McGill University Health Centre Research Institute, the heads of three healthy volunteers were scanned in the same MRI system as mentioned in section 2.1. CT scans of the volunteers were not obtained to avoid unnecessarily exposing them to radiation. The sCT images were qualitatively compared to the original MR images to verify that the anatomy of the subjects was correctly depicted.

Subject/sequence:	Phantom/PDw UTE	Volunteers
Voxel Size [mm^3]	1.1 × 1.1 × 1.5	1.1 × 1.1 × 1.5
FOV [cm^3]	24 × 24 × 19.2	25.6 × 25.6 × 19.2
TE1, TE2 [ms]	0.05	0.05, 4.54
TR [ms]	6	10
FA1, FA2 [°]	3, 13	3, 17
RO [ms]	0.840	1.240
Interleaves	500	200
Scan Time [min:sec]	3:40	2:07

Table 1: Pulse sequence parameters. Only the UTE sequence parameters are shown.

3. Results

3.1 Phantom Experiments

Qualitatively, the synthetic and X-ray CT images look very similar. In Figure 3a and 3b, the agar phantom has the same shape, and the air cavity in the empty piece of bone has the same shape in both scans. The same blood vessel can be observed in the piece of bone containing marrow. In Figure 3d and 3e, CT numbers of fat were correctly assigned inside the fresh piece of femur on the sCT, and bumps can be seen inside the empty piece of bone at the same position as on X-ray CT.

Most differences between the synthetic and X-ray CT were found at the interfaces between different materials, as shown in Figure 3c and 3f, which compares synthetic and X-ray CT images and shows the difference in HU between the two volumes. Plastic components such as the piece of polyoxymethylene and the phantom container, as well as the scanner couch, are invisible on MRI, and thus are not represented on the sCT. The foam pads used to immobilize the phantom in the head coil produced some signal on MR, which was interpreted as partial volume voxels by the sCT algorithm, resulting in CT numbers slightly higher than air (average of -959 HU, maximum of -890 HU) on one side of the phantom. In Figure 3a through c, we can see how the fat shift at the interface between bone and bone marrow in the fresh piece of bone leads to a misidentification of bone as fat, and thus an increase in the bone's inner radius.

Quantitative comparison of the synthetic and X-ray CT revealed a good correlation between CT and sCT numbers, with especially good sensitivity and specificity for bone voxels, and decent results for other materials. These results are reported in Table 2. For the whole volume shown in the images of Figure 3, the ICC indicates that there is a good correlation between the CT numbers of both images. The algorithm has both high sensitivity and specificity to bone. For air, the algorithm has lower specificity due to the greater number of false positives, which is unsurprising since the plastic container and the scanner table were both invisible on MRI, and because the inner surface of the empty piece of femur was eroded on the sCT images. The algorithm also appears to have lower sensitivity to agar and fat. However, this does not include the voxels segmented as mixtures of agar and air since these can also be found outside the phantom has explained earlier. Including these increases the sensitivity to agar and fat to 0.75 but lowers the specificity to 0.90 because of the greater number of false positives. This ambiguity results in a lower DSC than in bone and in air but does not necessarily imply worse performance in terms of CT number assignment as evidenced by the ICC of 0.82 and MAE of 123 HU.

Synthetic and X-ray CT numbers correlate well across air, fat, agar, and bone, as depicted in Figure 4. The most evident deviation from the ideal scenario, represented by the dotted blue line, is found for CT numbers smaller than 0 HU in both scans, presumably in voxels partially composed of air. The misassignment of CT numbers to the piece of Delrin can be found above this region, highlighted by a green box. There are two perfectly vertical lines observed at 0 HU and -70 HU due to the misassignment of bulk CT numbers to various materials in the phantom. A horizontal line can be observed around CT numbers of 0 HU because some fat and agar voxels were assigned air or bone sCT numbers. There is not enough variability in the density of the pieces of femur to ascertain the linearity between sCT and CT in bone alone.

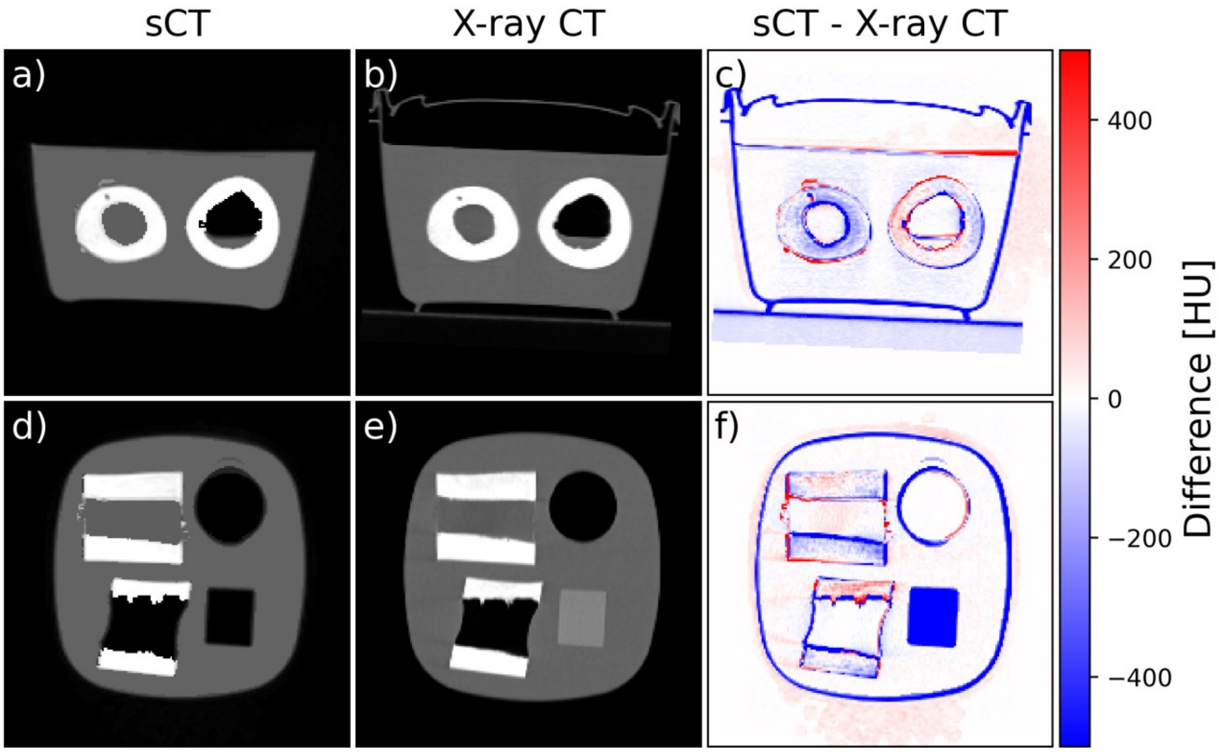

Figure 3: Comparison of synthetic CT and X-ray CT in a phantom. The sCT and CT of two different cross-sections of a home-made phantom are compared. The phantom features (from left to right, top to bottom, in e)) a fresh piece of bovine femur containing marrow, a ping pong ball acting as an air cavity, a piece of bovine femur which was emptied of marrow, cleaned, and rehydrated, and a piece of polyoxymethylene (Delrin®) to create an area of magnetic resonance signal void with less distortion than air due to susceptibility artifacts. The difference image between the sCT and the CT is shown in the last column of the figure.

Metric	Whole Volume	Bone	Air	Agar and Fat
ME [HU]	-32	-147	3	-104
MAE [HU]	46	222	7	123
ICC	0.95	0.57	0.00	0.82
Sensitivity	NA	0.92	0.98	0.66
Specificity	NA	1.00	0.75	1.00
DSC	NA	0.93	0.94	0.79

Table 2: Quantitative evaluation of the CT numbers of the sCT and X-ray CT. The mean error (ME), mean absolute error (MAE), and the interclass correlation coefficient (ICC) were computed from the HU of the sCT and CT to evaluate the CT number assignment. The segmentation aspect of the algorithm was assessed by calculating the sensitivity, specificity, and Dice's similarity coefficient for masks of bone, air, and agar and fat.

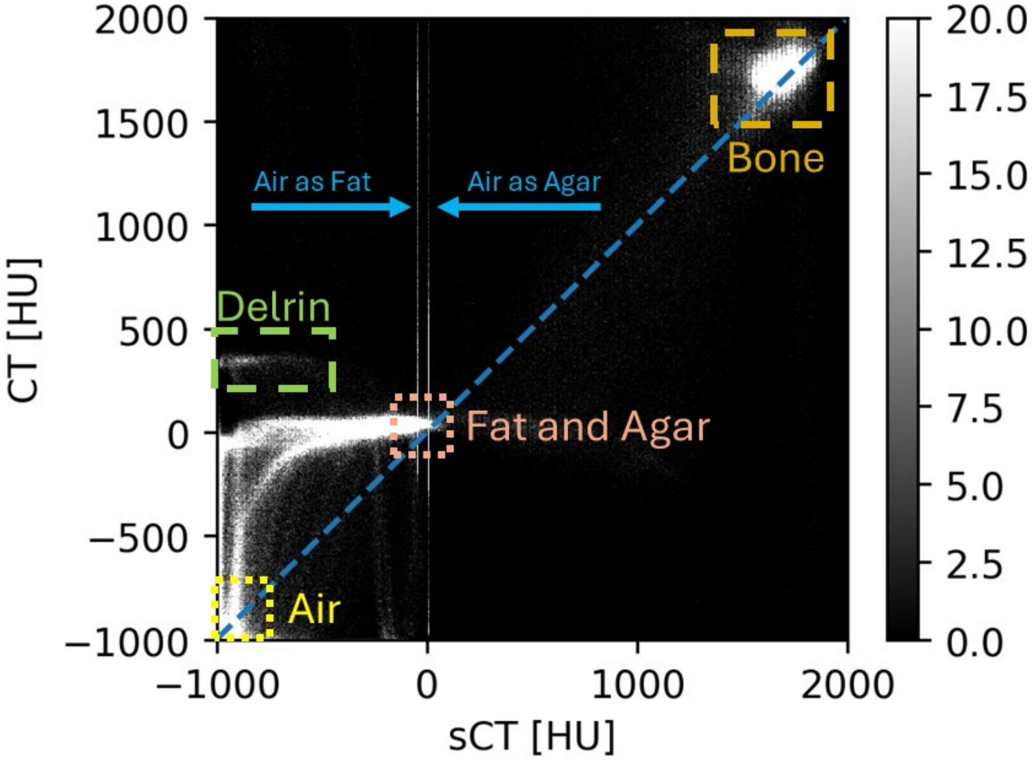

Figure 4: Hounsfield units of each voxel in the X-ray CT and synthetic CT. This two-dimensional histogram presents the voxel values of paired voxels in both scans, showing sCT numbers on the x-axis and X-ray CT numbers on the y-axis. A perfect correlation would follow the dotted blue line. The lower left quadrant of the graph (-1000 HU to 0 HU in both X-ray CT and sCT) suggest that the handling of partial volume voxels needs improvement.

3.2 In Vivo Experiments

In vivo, the anatomy visible on sCT corresponds well to the anatomy observed on the bone-optimized images, as shown in Figure 5. The major bones of the head are visible in the sCT images. The algorithm can distinguish bone from air in the sinuses, the nasal cavity, and the mastoid air cells. Fat that appears bright on MRI is accurately segmented. However, fat voxels that appear darker on MRI are misidentified as bone, as observed in the subcutaneous fat on the back of the neck, under the chin, and on top of the cranium.

Partial volumes of air and soft tissue were handled adequately such that there are very few voxels with high CT numbers in the nasal cavity or the larynx and pharynx on the synthetic CT. Unfortunately, this was an issue at the back of the neck because a signal was detected from the foam pad used for immobilization (Figure 5c). As a result, voxels of air on CT were assigned sCT numbers of 1800 HU instead of -1000 HU.

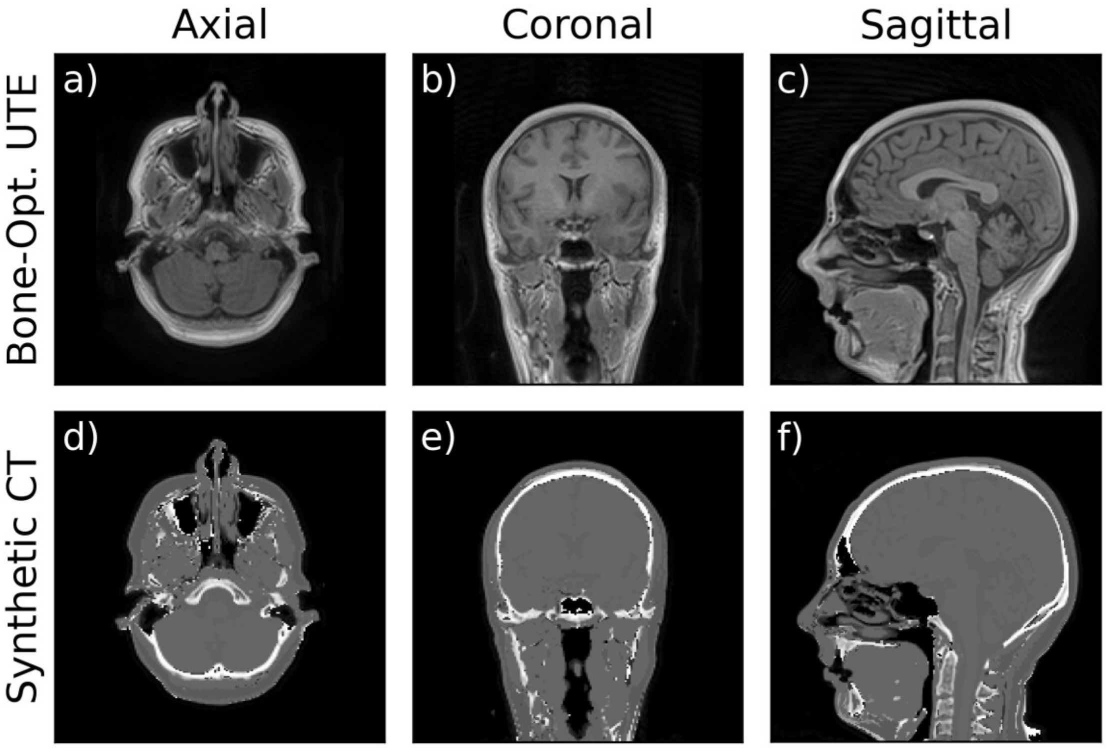

Figure 5: Qualitative assessment of *in vivo* synthetic CT images. The sCT images of the head of a volunteer are shown below the bone-optimized images that were used in the algorithm. In general, the sCT images have a plausible appearance and the algorithm differentiated between air and bone in most cases. However, certain fat voxels were segmented as bone, as seen in all cross-sections. In the axial slice, mastoid air cells are visible, although with poor resolution. In the coronal cross-section, the bony wall of the sphenoid sinus is visible. In the sagittal sCT, details in the nasal cavity are preserved, with very few voxels appearing as cortical bone due to partial volume effects.

4. Discussion

The algorithm proposed in this work can produce sCT images with plausible appearance in both simple phantoms and human heads. In the case of the phantom, apart from plastic components, the different materials were adequately segmented and assigned CT numbers.

The MAE on sCT numbers suggests that the algorithm proposed here outperforms most methods proposed in literature covered by these recent systematic reviews[7,34]. However, these techniques were tested in patient cohorts, whose anatomies are much more complex than the phantom used in our study. A similar phantom study was conducted by Ghose *et al.*, in which a CT synthesis algorithm based on a random forest regression was tested in two porcine legs[35]. Although better MAEs (91 HU for bone) were reported, their phantoms did not feature air cavities and plastic structures. Moreover, the algorithm proposed in this paper was not tested in human volunteers.

In the phantom, most errors identified on the difference map between X-ray CT and sCT were found at the edges of different materials. This is likely caused by registration errors. The sCT images were difficult to register to X-ray CT potentially due to geometrical distortions occurring on MRI. The stack-of-spirals sequence used for this project does not feature distortion or off-resonance corrections, which have been shown to impact the shape of objects in MRI[36,37].

To achieve a reasonable scan time, the number of phase encoding steps was kept low by setting the readout time to 1.240 ms. In pulse sequences with center-out k-space trajectories, longer readout times lead to lower spatial resolutions in short T2* objects[38]. Longer readout times also yield to increased fat-shifts[39].

The ICC measures how closely sCT and X-ray CT numbers follow a one-to-one relationship. This was the case overall in our results, showing high ICC. However, for CT numbers between -1000 HU and 10 HU, the sCT numbers were lower than the X-ray CT numbers. This suggests that the equation used to assign CT numbers to voxels partially composed of air and agar could be improved. However, the plastic container, which has CT numbers similar to agar, extends the visible width of the phantom on CT because it is invisible on MRI, leading to higher CT numbers on the outer edges of the phantom on X-ray CT compared to sCT.

The ICC of bone voxel values was low due to the low variability in bone density in the bone sample (1500 HU to 2000 HU), when compared to the noise in both synthetic and X-ray CT. If any, further phantom studies should be carried out with a wider range of bone densities to assess the linearity of sCT and CT numbers in bone.

The ICC of air was 0.00 because there was more variability in the CT numbers of air regions of the sCT than expected. This was partly caused by the signal detected from the immobilization foam pads on the sides of the phantom, which were segmented as air-agar mixtures and assigned CT numbers as high as -800 HU. Moreover, by the time the phantom was scanned using MRI, water had pooled at the surface of the phantom and inside the empty piece of femur. Hence, in the ICC calculation, the CT numbers of some voxels segmented as agar were compared to ones of air voxels on X-ray CT.

The high sensitivity for air and bone was possible thanks to the incorporation of the bone-optimized images. In Figure 1b, the frontal sinus can be delineated with ease. The low specificity for air and low sensitivity for agar and fat are consequences of numerous false positives for air and false negatives for agar and fat, respectively. These are both consequences of the visibility of plastic on X-ray CT, which was classified as air on sCT.

In vivo, most erroneous sCT number assignments were caused by the misidentification of fat voxels as bone, probably caused by the similarity in colour of the two species in the constructed RGB image. Optimizing the contrast of the input images could improve the output of the algorithm. So far, the pulse sequence parameters used have not been optimized to create the greatest colour differences between tissues. Simulations of MR signals could be performed with known T1, T2* and PD of various tissues to optimize the sequence parameters to obtain input images most likely to be correctly segmented. The current parameters were chosen based on the hypothesis, in addition to a PDw UTE image for CT number calculations for bone, the algorithm would need an image with as much bone signal as possible for good air-bone differentiation, and an image without bone signal to differentiate bone from other tissues.

5. Conclusion

This work demonstrated the use of deterministic colour image segmentation methods on RGB images composed of MRI acquisitions with different contrasts to differentiate between various types of tissues to create sCT images. The method proposed in this work can still be improved by optimizing the contrast of input images and by improving on the current use of the RAG. The algorithm’s capacity to generate images in both the phantom and heads of human volunteers suggest that it should be easily adapted to different parts of the anatomy. The next step will be to use the algorithm in other parts of the anatomy and to recruit patients from whom X-ray CT images can be collected and compared against sCT.

6. Acknowledgments

We wish to thank the Montreal General Hospital MRI Research Platform and the McGill University Health Center for granting access to the scanners used in this project. This work has also made use of Scikit-Image v0.22.0 (SLIC and RAG), and fuzzy-c-means v1.7.0, which are free and open-source Python packages. We also want to acknowledge the help of Renée-Claude Bider and Jorge Campos Pazmino for their expertise in agar-based phantom fabrication, and Joe Larkin and Boucherie Vito for experimental materials.

References

1. Johnstone E, Wyatt JJ, Henry AM, et al. Systematic Review of Synthetic Computed Tomography Generation Methodologies for Use in Magnetic Resonance Imaging–Only Radiation Therapy. *International Journal of Radiation Oncology*Biology*Physics*. 2018/01/01/ 2018;100(1):199-217. doi:https://doi.org/10.1016/j.ijrobp.2017.08.043
2. Speight R, Tyyger M, Schmidt MA, et al. IPEM Topical Report: an international IPEM survey of MRI use for external beam radiotherapy treatment planning. *Physics in Medicine & Biology*. 2021/03/23 2021;66(7):075007. doi:10.1088/1361-6560/abe9f7
3. Thomas SJ. Relative electron density calibration of CT scanners for radiotherapy treatment planning. *British Journal of Radiology*. 1999;72(860):781-786. doi:10.1259/bjr.72.860.10624344
4. Ulin K, Urie MM, Cherlow JM. Results of a Multi-Institutional Benchmark Test for Cranial CT/MR Image Registration. *International Journal of Radiation*

*Oncology*Biology*Physics*. 2010/08/01/ 2010;77(5):1584-1589. doi:https://doi.org/10.1016/j.ijrobp.2009.10.017

5. Hanvey S, Sadozye AH, McJury M, Glegg M, Foster J. The influence of MRI scan position on image registration accuracy, target delineation and calculated dose in prostatic radiotherapy. *British Journal of Radiology*. 2012;85(1020):e1256-e1262. doi:10.1259/bjr/26802977

6. Jonsson J, Nyholm T, Söderkvist K. The rationale for MR-only treatment planning for external radiotherapy. *Clinical and Translational Radiation Oncology*. 2019/09/01/ 2019;18:60-65. doi:https://doi.org/10.1016/j.ctro.2019.03.005

7. Sherwani MK, Gopalakrishnan S. A systematic literature review: deep learning techniques for synthetic medical image generation and their applications in radiotherapy. Systematic Review. *Frontiers in Radiology*. 2024;4

8. Wiesinger F, Bylund M, Yang J, et al. Zero TE-based pseudo-CT image conversion in the head and its application in PET/MR attenuation correction and MR-guided radiation therapy planning. *Magnetic Resonance in Medicine*. 2018/10/01 2018;80(4):1440-1451. doi:https://doi.org/10.1002/mrm.27134

9. Su K-H, Friel HT, Kuo J-W, et al. UTE-mDixon-based thorax synthetic CT generation. *Medical Physics*. 2019/08/01 2019;46(8):3520-3531. doi:https://doi.org/10.1002/mp.13574

10. Fortier V, Fortin M-A, Pater P, Souhami L, Levesque IR. A role for magnetic susceptibility in synthetic computed tomography. *Physica Medica*. 2021/05/01/ 2021;85:137-146. doi:https://doi.org/10.1016/j.ejmp.2021.05.001

11. Dowling JA, Lambert J, Parker J, et al. An Atlas-Based Electron Density Mapping Method for Magnetic Resonance Imaging (MRI)-Alone Treatment Planning and Adaptive MRI-Based Prostate Radiation Therapy. *International Journal of Radiation Oncology*Biology*Physics*. 2012/05/01/ 2012;83(1):e5-e11. doi:https://doi.org/10.1016/j.ijrobp.2011.11.056

12. Farjam R, Tyagi N, Deasy JO, Hunt MA. Dosimetric evaluation of an atlas-based synthetic CT generation approach for MR-only radiotherapy of pelvis anatomy. *Journal of Applied Clinical Medical Physics*. 2019/01/01 2019;20(1):101-109. doi:https://doi.org/10.1002/acm2.12501

13. Demol B, Boydev C, Korhonen J, Reynaert N. Dosimetric characterization of MRI-only treatment planning for brain tumors in atlas-based pseudo-CT images generated from standard T1-weighted MR images. *Medical Physics*. 2016/12/01 2016;43(12):6557-6568. doi:https://doi.org/10.1118/1.4967480

14. Tang B, Wu F, Fu Y, et al. Dosimetric evaluation of synthetic CT image generated using a neural network for MR-only brain radiotherapy. *Journal of Applied Clinical Medical Physics*. 2021/03/01 2021;22(3):55-62. doi:https://doi.org/10.1002/acm2.13176

15. Jabbarpour A, Mahdavi SR, Vafaei Sadr A, Esmaili G, Shiri I, Zaidi H. Unsupervised pseudo CT generation using heterogenous multicentric CT/MR images and CycleGAN: Dosimetric assessment for 3D conformal radiotherapy. *Computers in Biology and Medicine*. 2022/04/01/ 2022;143:105277. doi:https://doi.org/10.1016/j.compbiomed.2022.105277

16. Sun H, Xi Q, Fan R, et al. Synthesis of pseudo-CT images from pelvic MRI images based on an MD-CycleGAN model for radiotherapy. *Physics in Medicine & Biology*. 2022/01/28 2022;67(3):035006. doi:10.1088/1361-6560/ac4123

17. Chopra KL, Leo P, Kabat C, et al. Evaluation of dose calculation accuracy of treatment planning systems in the presence of tissue heterogeneities. *Therapeutic Radiology and Oncology*. 2018;2

18. Hsu S-H, Cao Y, Lawrence TS, et al. Quantitative characterizations of ultrashort echo (UTE) images for supporting air–bone separation in the head. *Physics in Medicine & Biology*. 2015/03/17 2015;60(7):2869. doi:10.1088/0031-9155/60/7/2869

19. Johansson A, Karlsson M, Nyholm T. CT substitute derived from MRI sequences with ultrashort echo time. *Medical Physics*. 2011/05/01 2011;38(5):2708-2714. doi:https://doi.org/10.1118/1.3578928

20. Koivula L, Seppälä T, Collan J, Visapää H, Tenhunen M, Korhonen A. Synthetic computed tomography based dose calculation in prostate cancer patients with hip prostheses for magnetic resonance imaging-only radiotherapy. *Physics and Imaging in Radiation Oncology*. 2023/07/01/ 2023;27:100469. doi:https://doi.org/10.1016/j.phro.2023.100469

21. Juttukonda MR, Mersereau BG, Chen Y, et al. MR-based attenuation correction for PET/MRI neurological studies with continuous-valued attenuation coefficients for bone through a conversion from R2* to CT-Hounsfield units. *NeuroImage*. 2015/05/15/ 2015;112:160-168. doi:https://doi.org/10.1016/j.neuroimage.2015.03.009

22. Lustig M, Pauly JM. SPIRiT: Iterative self-consistent parallel imaging reconstruction from arbitrary k-space. *Magnetic Resonance in Medicine*. 2010/08/01 2010;64(2):457-471. doi:https://doi.org/10.1002/mrm.22428

23. Tustison NJ, Avants BB, Cook PA, et al. N4ITK: Improved N3 Bias Correction. *IEEE Transactions on Medical Imaging*. 2010;29(6):1310-1320. doi:10.1109/TMI.2010.2046908

24. Achanta R, Shaji A, Smith K, Lucchi A, Fua P, Süsstrunk S. SLIC Superpixels Compared to State-of-the-Art Superpixel Methods. *IEEE Transactions on Pattern Analysis and Machine Intelligence*. 2012;34(11):2274-2282. doi:10.1109/TPAMI.2012.120

25. Dunn JC. A Fuzzy Relative of the ISODATA Process and Its Use in Detecting Compact Well-Separated Clusters. *Journal of Cybernetics*. 1973/01/01 1973;3(3):32-57. doi:10.1080/01969727308546046

26. Fernandez-Maloigne C. *Advanced Color Image Processing and Analysis*. 1 ed. Springer New York, NY; 2012:VIII, 515.

27. Hsin-Chia C, Wei-Jung C, Sheng-Jyh W. Contrast-based color image segmentation. *IEEE Signal Processing Letters*. 2004;11(7):641-644. doi:10.1109/LSP.2004.830116

28. Tremeau A, Colantoni P. Regions adjacency graph applied to color image segmentation. *IEEE Transactions on Image Processing*. 2000;9(4):735-744. doi:10.1109/83.841950

29. Khalifé M, Fernandez B, Jaubert O, et al. Subject-specific bone attenuation correction for brain PET/MR: can ZTE-MRI substitute CT scan accurately? *Physics in Medicine & Biology*. 2017/09/20 2017;62(19):7814. doi:10.1088/1361-6560/aa8851

30. Duan Q, Duyn JH, Gudino N, et al. Characterization of a dielectric phantom for high-field magnetic resonance imaging applications. *Medical Physics*. 2014/10/01 2014;41(10):102303. doi:https://doi.org/10.1118/1.4895823

31. Bush EC, Gifford A, Coolbaugh CL, Towse TF, Damon BM, Welch EB. Fat-Water Phantoms for Magnetic Resonance Imaging Validation: A Flexible and Scalable Protocol. *JoVE*. 2018/09/07 2018;(139):e57704. doi:doi:10.3791/57704

32. Soliman AS, Burns L, Owrangi A, et al. A realistic phantom for validating MRI-based synthetic CT images of the human skull. *Medical Physics*. 2017/09/01 2017;44(9):4687-4694. doi:https://doi.org/10.1002/mp.12428

33. Tse ZTH, Elhawary H, Montesinos CAF, Rea M, Young I, Lamperth M. Testing MR image artifacts generated by engineering materials. *Concepts in Magnetic Resonance Part B:*

Magnetic Resonance Engineering. 2011/04/01 2011;39B(2):109-117. doi:https://doi.org/10.1002/cmr.b.20197

34. Villegas F, Dal Bello R, Alvarez-Andres E, et al. Challenges and opportunities in the development and clinical implementation of artificial intelligence based synthetic computed tomography for magnetic resonance only radiotherapy. *Radiotherapy and Oncology*. 2024/09/01/ 2024;198:110387. doi:https://doi.org/10.1016/j.radonc.2024.110387

35. Ghose S, Dowling JA, Rai R, Liney GP. Substitute CT generation from a single ultra short time echo MRI sequence: preliminary study. *Physics in Medicine & Biology*. 2017/03/17 2017;62(8):2950. doi:10.1088/1361-6560/aa508a

36. Weygand J, Fuller CD, Ibbott GS, et al. Spatial Precision in Magnetic Resonance Imaging–Guided Radiation Therapy: The Role of Geometric Distortion. *International Journal of Radiation Oncology*Biology*Physics*. 2016/07/15/ 2016;95(4):1304-1316. doi:https://doi.org/10.1016/j.ijrobp.2016.02.059

37. Haskell MW, Nielsen J-F, Noll DC. Off-resonance artifact correction for MRI: A review. *NMR in Biomedicine*. 2023/05/01 2023;36(5):e4867. doi:https://doi.org/10.1002/nbm.4867

38. Robison RK, Anderson Iii AG, Pipe JG. Three-dimensional ultrashort echo-time imaging using a FLORET trajectory. *Magnetic Resonance in Medicine*. 2017/09/01 2017;78(3):1038-1049. doi:https://doi.org/10.1002/mrm.26500

39. Engström M, McKinnon G, Cozzini C, Wiesinger F. In-phase zero TE musculoskeletal imaging. *Magnetic Resonance in Medicine*. 2020/01/01 2020;83(1):195-202. doi:https://doi.org/10.1002/mrm.27928

Chapter 5: Discussion

This chapter expands on the discussion of the manuscript presented in Chapter 5. First, certain parameter choices, pulse sequence limitations, and solutions to address these constraints will be covered. Second, the potential role of UTE in RTP beyond CT synthesis will be discussed. Third, potential refinements to the segmentation pipeline will be considered. Finally, the difficulties surrounding partial volume effects will be addressed.

5.1 Considerations for Image Acquisition

5.1.1 Readout duration and trajectory

With the spiral sequence used in this work, using longer readout durations increased the sampling efficiency and greatly reduced scan time. Spiral imaging struggles with quick readouts[23] because the rate of change of the gradient field is limited, either by the scanner's capabilities, or by the likelihood of inducing eddy currents in the patient's body, leading to unwanted peripheral nerve stimulation (PNS)[19]. This entails that the maximum curvature of a spiral interleave is limited by the speed at which the k-space is travelled in[24,115], and thus by the readout duration. Shorter interleaves sample fewer points in k-space and thus more interleaves are necessary to fully sample the Fourier domain. For our sequence specifically, the number of interleaves needed to fully sample the Fourier domain increases exponentially with the inverse of the readout duration. Lowering the readout duration to 0.8 ms – the lowest value possible with our sequence – increased the acquisition time of the bone optimized sequence to 7 minutes 40 seconds. By comparison, a scan with a readout duration of 1.24 ms lasts 2 minutes 7 seconds.

Unfortunately, longer readouts lower spatial resolution, which is especially noticeable for short T_2* tissues because their signals can decay substantially before the high frequency contents of k-space are sampled[18]. Blurry edges between bone and air can lead to the erroneous representation of the boney walls of sinuses. Resolution is also limited by the shape of the spirals used[25]. Our stack-of-spiral sequence uses a "dual-density" trajectory[116]. Using the definitions of Delattre *et al.*[24], this approach uses spirals of unit density with a varying FOV. This is to sample twice as much data in the center of k-space compared to the outer region, thus enabling auto-calibration calculations in GRAPPA-based reconstructions[117] that greatly reduce scan duration. The side-effect of this trajectory is that more time is spent sampling the low-frequency contents of k-space, instead of the mid and high-frequency contents. A cones-based sequence with sub-unit density such as FLORET could allow us to read the higher-frequency content of k-space sooner[25], improving the sharpness of the edges between bone and air found in sinuses.

Besides degrading spatial resolution, longer readout durations lead to a greater spiral fat-shift artifact. This phenomenon presents itself as a dark edge around the fat regions and has been documented for radial acquisitions in Engström *et al.*[118]. Fat-water separation could be considered to correct fat-shifts[119], but this would necessitate the acquisition of three or more echoes at spacings that are not feasible in a single repetition, implying that more scans would be needed. Engström *et al.* proposed a method to correct for chemical shift interference in in-phase ZTE imaging which could be adapted to any center-out sequence, such as our stack-of-spirals, with no time penalty[118].

5.1.2 Replacing MPRAGE Images with a Second Echo

Earlier versions of the algorithm relied on an additional MPRAGE image instead of the second echo of the bone-optimized sequence. In the initial development of the method, we hypothesized that a T1w image that would be routinely acquired in the clinic for RTP could be reused in the CT synthesis algorithm to obtain a third, boneless image, without further increasing scan time. The MPRAGE acquisition acted as this clinical image. In reality, since the exact T1w sequence, and thus contrast, used for RTP varies from one hospital to another[41], the performance of the algorithm could have varied across centers. Using a second echo with known contrast ensures the consistency of the algorithm without increasing the required scan time, allowing the center to use whichever T1w image they want for RTP.

The second echo also acted as a temporary fix for geometrical distortions. Since the spiral sequence used in this work does not feature geometrical distortion corrections yet, large objects (relative to the FOV) seem stretched at the superior and inferior extremities on spiral images. This is not the case for MPRAGE images which feature distortion corrections. Since the algorithm requires the three input images to be aligned, the spiral images had to be manually registered to the MPRAGE, introducing errors in the final sCT image and defeating the purpose of MR-only RTP.

Unfortunately, using a second echo in the spiral sequence also has disadvantages. The likelihood for PNS is increased by using a second echo such the usage of gradient fields is doubled per repetition[120]. In terms of the algorithm's performance, the second echo provides a weaker fat signal in the red channel of the colour image compared to the MPRAGE, making fat harder to segment from bone.

5.1.3 A Role for UTE in RTP

Using short echo times has the benefit of reducing the severity of susceptibility artifacts[121]. On many MR images, tissues surrounding air cavities , bones or implants are engulfed in a signal void which grows as the echo time is increased. With a TE of 50 µs, these signal voids are not noticeable, and therefore propagate to a lesser extent to the sCT images, insuring greater geometric fidelity. This suggests that using UTE imaging could be beneficial for RTP accuracy outside of CT synthesis. Since rigid registration is commonly used to align MR images to a planning CT[42], distortions in targets on MRI are propagated as errors in contours to the treatment plan[122]. If T1w and T2w UTE[123] images with adequate geometrical distortion corrections could be acquired instead of the standard clinical sequences used for RTP, contours on MRI would be more accurate to the true shapes of targets, thus lowering the geometrical error in the CT-based dose calculation.

5.1.4 Imaging Non-tissue Materials

On CT-simulator images, it is useful to visualize fixation devices for accurate dose calculations, either to directly compute the dose they absorb or to place a predefined device with accurate CT numbers[124]. While these objects with little to no free protons can easily be observed on CT, they do not appear on conventional MRI, or on the subsequent sCT images, as was the case for the plastic container around our phantom. For MR-only planning to be sustainable, non-tissue materials will have to be detected[125]. UTE and ZTE sequences with extremely short readout durations (around 0.25 ms) are capable of imaging plastic[20] (*e.g.* the outer shell of receive coils) and rubber. Foam can be imaged with longer readouts as demonstrated in our own images. This basic visualization could help dosimetrists to insert predefined models for fixation devices as it is currently done for treatment couches on CT images. Alternatively, markers visible on MRI could be used on rigid devices to allow dosimetrists to align predefined models, but soft bolus would be hard to define in the treatment plan based on a handful of markers.

Since our algorithm can synthesize CT images of phantoms, we can imagine that it would be possible to carry phantom-based quality assurance testing (QA) to monitor the accuracy of the geometry and CT numbers of our synthetic CT images. Soliman *et al.* assembled a phantom using a rehydrated *ex vivo* skull with the purpose of validating synthetic CT algorithms[126]. However, they measured a T_2* for cortical bone that was twice as long as *in vivo* at 3T, suggesting that cortical bone would be easier to image when *ex vivo* and cleaned. Chandramohan *et al.* tested alternatives for bone in multimodal phantoms, notably for PET/MR[127]. As discussed in that work, by doping plaster with Iodine, a gadolinium-based contrast agent and copper sulfate, objects with similar T_1, T_2* and radiation attenuation as *in vivo* bone could be built. This kind of phantom could be used for sCT/CT comparisons and sCT quality assurance testing. For our own work, this suggests that further phantom studies should be carried out using doped plaster rather than *ex vivo* bone segments to obtain accurate MR signals.

5.2 Potential Improvement of the Algorithm

The quality of the sCT images depends mainly on the correct segmentation of the colour image. For this reason, focusing on improving the segmentation should be the first step towards accurate sCT images.

5.2.1 Potential Improvements

In its current form, our use of the RAG is underdeveloped. There are several graph-based methods known to perform better than thresholding, such as watersheds[128], mean cuts[129], ratio cuts[130], and normalized cuts[131]. Bejar *et al.* proposed a technique based on optimum oriented cuts which is robust to illumination variations and inhomogeneity effects on superpixels obtained using a SLIC-based method[132]. This would make our segmentation more accurate in regions with variations in signal intensity that were not corrected by the N4ITK bias field correction, as seen in the subcutaneous fat depicted in Figure 5c of Chapter 4. In the case of the fat under the chin, better robustness to inhomogeneous intensity could have prevented fat voxels from being identified as bone.

The primary purpose of the final segmentation step relying on FCM is to constrain the final number of masks to the number of tissues we expect to observe in CT. K-means and FCM clustering are methods that perform better with globular clusters of similar sizes[32], as described in Section 2.5.2. However, we do not expect the clusters to have comparable sizes because there should be more soft-tissue voxels than bone. DBSCAN[133], HDBSCAN[134] and OPTICS[135] are well-known examples of clustering algorithms that perform very well with clusters of different sizes and shapes. However, unlike K-means and FCM, none of these algorithms can use a predefined number of clusters. Ward hierarchical clustering needs a user-specified number of clusters and can handle clusters of different sizes, but they still need to be globular[136]. Hence, Ward's method has the potential to increase the performance of the last step of our segmentation technique.

Since using a dual echo sequence does not extend the scan time, a second echo of the PDw UTE image could be acquired and used in the algorithm to increase the amount of information for the segmentation since SLIC, RAG thresholding, and FCM clustering can be extended to N-channel images. However, in our current usage of SLIC and FCM clustering, the RGB image is constructed from three MR images and converted to the CIELAB colour space, a space that better represents human perception of colour, before segmentation. This conversion increases the performance of the segmentation[137]. But the conversion from RGB to CIELAB, limited to three-channel images, prohibits the use of four channel-images. Future work could explore ways to incorporate a fourth MR image instead of using the CIELAB colour space.

5.2.3 Partial Volume Voxels

The multi-channel approach presented in this work adequately handles partial volume voxels of air and water-based soft tissue inside the head in areas such as the nasal cavity. This is because these pixels are easily clustered in the FCM based on their dark green colour. This strategy cannot be used for partial volume voxel of fat and water-based soft tissue, and bone and soft-tissue because the colours of these mixtures are similar. In these cases, SLIC sets a hard boundary between tissues.

Since numerous voxels are mixtures of tissues, describing them in terms of mixtures of materials could be beneficial to CT synthesis by improving the accuracy of sCT numbers assigned to partial volume voxels. Some research groups have attempted to use mixtures such as gaussian regressions[79] or FCM[10,110] to assign CT numbers. These techniques use clusters with centroids, and the mixtures are determined using the distance a point has from all centroids. So far, our usage of the FCM was restricted to the use of binary masks, similar to the output of k-means clustering. The fuzzy outputs of the FCM method could allow us to represent mixtures of tissues and obtain sCT numbers that are more representative of edges.

Chapter 6: Conclusion

6.1 Summary

In this work, a novel CT synthesis method based on UTE MRI and deterministic colour image segmentation techniques was proposed to address the need for a simple sCT algorithm relying on rapidly-acquired images and without assumptions about patient anatomy.

First, a UTE sequence featuring interleaved spiral k-space trajectories was successfully deployed and optimized to be used in the sCT algorithm developed alongside. The MR images were merged into colour images from which tissues relevant to sCT in RTP could be segmented using well-established colour image segmentation methods. The masks generated by the segmentation and pixel values from a PDw image were used in the assignment of sCT numbers. This method proved to be quantitatively accurate in a phantom and easy to implement in imaging the human head, where qualitatively plausible sCT images were produced. The main limitation of the algorithm is the erroneous detection of bone voxels in fat regions, probably caused by fat shift artifacts.

6.2 Future Study

Further study should investigate the impact that potential improvements proposed in Chapter 5 could have on the quality of the sCT images. The first idea to test would be to use more elaborate RAG methods such as optimum oriented cuts[132]. This could lead to fewer fat voxels being recognized as bone, without eliminating fat-shifts through increased scan times[23] or implementing highly specialized reconstruction methods[118]. Fixing this issue in the segmentation would reduce the volume of erroneously segmented bone, which is considered one of the main failure points of MR-only RTP[60].

The sCT algorithm should also be tested to confirm that it can easily be adapted to various other parts of the anatomy. Given the interest in MR-only RTP for prostate cancer[104,138,139], the pelvis could be the next site of interest. Limbs could be targets for further testing because they are relatively easy to scan; motion is easily avoided and specialized receiver coils have been designed for ankles, knees, and shoulders. The head-and-neck, abdomen and thorax will probably be the most challenging sites to image because of breathing motion[108,111]. Special techniques like breath-hold imaging or navigators[140] will have to be used to test the sCT algorithm in these regions.

The technique should be prospectively tested on patients, for whom X-ray CT scans and treatment plans exist and could be used for quantitative assessment. CT images would be used for quantitative CT number comparisons between X-ray and synthetic CT much like ones carried out in phantom and presented in Chapter 4. With treatment plans, the dose could be calculated using the sCT images and compared against the dose obtained from X-ray CT. This comparison would better reflect how errors in sCT numbers could affect treatment.

Bibliography

1. Podgorsak E. Radiation Oncology Physics: A Handbook for Teachers and Students. *British Journal of Cancer*. 2008/03/01 2008;98(5):1020-1020. doi:10.1038/sj.bjc.6604224

2. Herman GT. *Fundamentals of Computerized Tomography*. 2 ed. Advances in Computer Vision and Pattern Recognition. Springer; 2009:300.

3. Thomas SJ. Relative electron density calibration of CT scanners for radiotherapy treatment planning. *British Journal of Radiology*. 1999;72(860):781-786. doi:10.1259/bjr.72.860.10624344

4. Johnstone E, Wyatt JJ, Henry AM, et al. Systematic Review of Synthetic Computed Tomography Generation Methodologies for Use in Magnetic Resonance Imaging–Only Radiation Therapy. *International Journal of Radiation Oncology*Biology*Physics*. 2018/01/01/ 2018;100(1):199-217. doi:https://doi.org/10.1016/j.ijrobp.2017.08.043

5. Ulin K, Urie MM, Cherlow JM. Results of a Multi-Institutional Benchmark Test for Cranial CT/MR Image Registration. *International Journal of Radiation Oncology*Biology*Physics*. 2010/08/01/ 2010;77(5):1584-1589. doi:https://doi.org/10.1016/j.ijrobp.2009.10.017

6. Goodburn RJ, Philippens MEP, Lefebvre TL, et al. The future of MRI in radiation therapy: Challenges and opportunities for the MR community. *Magnetic Resonance in Medicine*. 2022/12/01 2022;88(6):2592-2608. doi:https://doi.org/10.1002/mrm.29450

7. Rickard O. Cronholm AK, Carl Siversson. MRI only radiotherapy planning using the transfer function estimation algorithm. https://www.spectronic.se/files/Whitepaper_TFE_202106.pdf

8. Michaela Hoesl NEC, Nilesh Mistry. MR-based Synthetic CT. An AI-based algorithm for continuous Hounsfield units in the pelvis and brain - with syngo.via RT Image Suite (VB60). https://www.magnetomworld.siemens-healthineers.com/publications/mreadings.

9. M. Köhler TV, M. Van Grootel, R. Hoogeveen, R. Kemppainen, S. Renisch. MR-only simulation for radiotherapy planning. White paper: Philips MRCAT for prostate dose calculations using only MRI data.

10. Fortier V, Fortin M-A, Pater P, Souhami L, Levesque IR. A role for magnetic susceptibility in synthetic computed tomography. *Physica Medica*. 2021/05/01/ 2021;85:137-146. doi:https://doi.org/10.1016/j.ejmp.2021.05.001

11. Hsu S-H, Cao Y, Lawrence TS, et al. Quantitative characterizations of ultrashort echo (UTE) images for supporting air–bone separation in the head. *Physics in Medicine & Biology*. 2015/03/17 2015;60(7):2869. doi:10.1088/0031-9155/60/7/2869

12. Achanta R, Shaji A, Smith K, Lucchi A, Fua P, Süsstrunk S. SLIC Superpixels Compared to State-of-the-Art Superpixel Methods. *IEEE Transactions on Pattern Analysis and Machine Intelligence*. 2012;34(11):2274-2282. doi:10.1109/TPAMI.2012.120

13. Tremeau A, Colantoni P. Regions adjacency graph applied to color image segmentation. *IEEE Transactions on Image Processing*. 2000;9(4):735-744. doi:10.1109/83.841950

14. McRobbie DW, Moore EA, Graves MJ. *MRI from Picture to Proton*. 3rd ed. Cambridge University Press; 2017. https://public.ebookcentral.proquest.com/choice/publicfullrecord.aspx?p=4829805

15. Robson MD, Gatehouse PD, Bydder M, Bydder GM. Magnetic Resonance: An Introduction to Ultrashort TE (UTE) Imaging. *Journal of Computer Assisted Tomography*. 2003;27(6)

16. Du J, Carl M, Bydder M, Takahashi A, Chung CB, Bydder GM. Qualitative and quantitative ultrashort echo time (UTE) imaging of cortical bone. *Journal of Magnetic Resonance*. 2010/12/01/ 2010;207(2):304-311. doi:https://doi.org/10.1016/j.jmr.2010.09.013

17. MacIntosh BJ, Graham SJ. Magnetic Resonance Imaging to Visualize Stroke and Characterize Stroke Recovery: A Review. Review. *Frontiers in Neurology*. 2013;4

18. Rahmer J, Börnert P, Groen J, Bos C. Three-dimensional radial ultrashort echo-time imaging with T2 adapted sampling. *Magnetic Resonance in Medicine*. 2006/05/01 2006;55(5):1075-1082. doi:https://doi.org/10.1002/mrm.20868

19. Schulte RF, Noeske R. Peripheral nerve stimulation-optimal gradient waveform design. *Magnetic Resonance in Medicine*. 2015/08/01 2015;74(2):518-522. doi:https://doi.org/10.1002/mrm.25440

20. Ljungberg E, Damestani NL, Wood TC, et al. Silent zero TE MR neuroimaging: Current state-of-the-art and future directions. *Progress in Nuclear Magnetic Resonance Spectroscopy*. 2021/04/01/ 2021;123:73-93. doi:https://doi.org/10.1016/j.pnmrs.2021.03.002

21. Zhou Z, Han F, Yan L, Wang DJJ, Hu P. Golden-ratio rotated stack-of-stars acquisition for improved volumetric MRI. *Magnetic Resonance in Medicine*. 2017/12/01 2017;78(6):2290-2298. doi:https://doi.org/10.1002/mrm.26625

22. Barger AV, Block WF, Toropov Y, Grist TM, Mistretta CA. Time-resolved contrast-enhanced imaging with isotropic resolution and broad coverage using an undersampled 3D projection trajectory. *Magnetic Resonance in Medicine*. 2002/08/01 2002;48(2):297-305. doi:https://doi.org/10.1002/mrm.10212

23. Robison RK, Anderson Iii AG, Pipe JG. Three-dimensional ultrashort echo-time imaging using a FLORET trajectory. *Magnetic Resonance in Medicine*. 2017/09/01 2017;78(3):1038-1049. doi:https://doi.org/10.1002/mrm.26500

24. Delattre BMA, Heidemann RM, Crowe LA, Vallée J-P, Hyacinthe J-N. Spiral demystified. *Magnetic Resonance Imaging*. 2010/07/01/ 2010;28(6):862-881. doi:https://doi.org/10.1016/j.mri.2010.03.036

25. Pipe JG, Zwart NR, Aboussouan EA, Robison RK, Devaraj A, Johnson KO. A new design and rationale for 3D orthogonally oversampled k-space trajectories. *Magnetic Resonance in Medicine*. 2011/11/01 2011;66(5):1303-1311. doi:https://doi.org/10.1002/mrm.22918

26. Cha MJ, Park HJ, Paek MY, et al. Free-breathing ultrashort echo time lung magnetic resonance imaging using stack-of-spirals acquisition: A feasibility study in oncology patients. *Magnetic Resonance Imaging*. 2018/09/01/ 2018;51:137-143. doi:https://doi.org/10.1016/j.mri.2018.05.002

27. Gurney PT, Hargreaves BA, Nishimura DG. Design and analysis of a practical 3D cones trajectory. *Magnetic Resonance in Medicine*. 2006/03/01 2006;55(3):575-582. doi:https://doi.org/10.1002/mrm.20796

28. Wiesinger F, Ho M-L. Zero-TE MRI: principles and applications in the head and neck. *British Journal of Radiology*. 2022;95(1136):20220059. doi:10.1259/bjr.20220059

29. Fernandez-Maloigne C. *Advanced Color Image Processing and Analysis*. 1 ed. Springer New York, NY; 2012:VIII, 515.

30. Saxena A, Prasad M, Gupta A, et al. A review of clustering techniques and developments. *Neurocomputing*. 2017/12/06/ 2017;267:664-681. doi:https://doi.org/10.1016/j.neucom.2017.06.053

31. MacQueen JB. Some methods for classification and analysis of multivariate observations. *Proceedings of 5th Berkeley Symposium on Mathematical Statistics and Probability*. 1967;1:281-297.

32. Raykov YP, Boukouvalas A, Baig F, Little MA. What to Do When K-Means Clustering Fails: A Simple yet Principled Alternative Algorithm. *PLOS ONE*. 2016;11(9):e0162259. doi:10.1371/journal.pone.0162259

33. Mittal H, Pandey AC, Saraswat M, Kumar S, Pal R, Modwel G. A comprehensive survey of image segmentation: clustering methods, performance parameters, and benchmark datasets. *Multimedia Tools and Applications*. 2022/10/01 2022;81(24):35001-35026. doi:10.1007/s11042-021-10594-9

34. Dunn JC. A Fuzzy Relative of the ISODATA Process and Its Use in Detecting Compact Well-Separated Clusters. *Journal of Cybernetics*. 1973/01/01 1973;3(3):32-57. doi:10.1080/01969727308546046

35. Sreenath Rao V, Eli S. Survey of contemporary trends in color image segmentation. *Journal of Electronic Imaging*. 10/1 2012;21(4):040901. doi:10.1117/1.JEI.21.4.040901

36. Samei EP, Norbert J. *Computed Tomography*. 1 ed. Springer Cham; 2019:XV, 470.

37. Barrett AM, S.; Dobbs, J.; Roques, T. *Practical Radiotherapy Planning*. 4 ed. CRC Press; 2009:432.

38. Mutic S, Palta JR, Butker EK, et al. Quality assurance for computed-tomography simulators and the computed-tomography-simulation process: Report of the AAPM Radiation Therapy Committee Task Group No. 66. *Medical Physics*. 2003/10/01 2003;30(10):2762-2792. doi:https://doi.org/10.1118/1.1609271

39. Chen W-ZX, Ying; Li, Jun. Impact of dose calculation algorithm on radiation therapy. *World J Radiol*. November 28, 2014 2014;6(11):874-880. doi:https://dx.doi.org/10.4329/wjr.v6.i11.874

40. Herrmann H, Seppenwoolde Y, Georg D, Widder J. Image guidance: past and future of radiotherapy. *Der Radiologe*. 2019/12/01 2019;59(1):21-27. doi:10.1007/s00117-019-0573-y

41. Speight R, Tyyger M, Schmidt MA, et al. IPEM Topical Report: an international IPEM survey of MRI use for external beam radiotherapy treatment planning. *Physics in Medicine & Biology*. 2021/03/23 2021;66(7):075007. doi:10.1088/1361-6560/abe9f7

42. Barber J, Yuen J, Jameson M, et al. Deforming to Best Practice: Key considerations for deformable image registration in radiotherapy. *Journal of Medical Radiation Sciences*. 2020/12/01 2020;67(4):318-332. doi:https://doi.org/10.1002/jmrs.417

43. Hanvey S, Sadozye AH, McJury M, Glegg M, Foster J. The influence of MRI scan position on image registration accuracy, target delineation and calculated dose in prostatic radiotherapy. *British Journal of Radiology*. 2012;85(1020):e1256-e1262. doi:10.1259/bjr/26802977

44. Jonsson J, Nyholm T, Söderkvist K. The rationale for MR-only treatment planning for external radiotherapy. *Clinical and Translational Radiation Oncology*. 2019/09/01/ 2019;18:60-65. doi:https://doi.org/10.1016/j.ctro.2019.03.005

45. Villegas F, Dal Bello R, Alvarez-Andres E, et al. Challenges and opportunities in the development and clinical implementation of artificial intelligence based synthetic computed tomography for magnetic resonance only radiotherapy. *Radiotherapy and Oncology*. 2024/09/01/ 2024;198:110387. doi:https://doi.org/10.1016/j.radonc.2024.110387

46. Sherwani MK, Gopalakrishnan S. A systematic literature review: deep learning techniques for synthetic medical image generation and their applications in radiotherapy. Systematic Review. *Frontiers in Radiology*. 2024;4

47. Masitho S, Szkitsak J, Grigo J, Fietkau R, Putz F, Bert C. Feasibility of artificial-intelligence-based synthetic computed tomography in a magnetic resonance-only radiotherapy workflow for brain radiotherapy: Two-way dose validation and 2D/2D kV-image-based positioning. *Physics and Imaging in Radiation Oncology*. 2022/10/01/ 2022;24:111-117. doi:https://doi.org/10.1016/j.phro.2022.10.002

48. Catana C, van der Kouwe A, Benner T, et al. Toward Implementing an MRI-Based PET Attenuation-Correction Method for Neurologic Studies on the MR-PET Brain Prototype. *Journal of Nuclear Medicine*. 2010;51(9):1431. doi:10.2967/jnumed.109.069112

49. Dayarathna S, Islam KT, Uribe S, Yang G, Hayat M, Chen Z. Deep learning based synthesis of MRI, CT and PET: Review and analysis. *Medical Image Analysis*. 2024/02/01/ 2024;92:103046. doi:https://doi.org/10.1016/j.media.2023.103046

50. Juttukonda MR, Mersereau BG, Chen Y, et al. MR-based attenuation correction for PET/MRI neurological studies with continuous-valued attenuation coefficients for bone through

a conversion from R2* to CT-Hounsfield units. *NeuroImage*. 2015/05/15/ 2015;112:160-168. doi:https://doi.org/10.1016/j.neuroimage.2015.03.009

51. Keereman V, Fierens Y, Broux T, De Deene Y, Lonneux M, Vandenberghe S. MRI-Based Attenuation Correction for PET/MRI Using Ultrashort Echo Time Sequences. *Journal of Nuclear Medicine*. 2010;51(5):812. doi:10.2967/jnumed.109.065425

52. Khalifé M, Fernandez B, Jaubert O, et al. Subject-specific bone attenuation correction for brain PET/MR: can ZTE-MRI substitute CT scan accurately? *Physics in Medicine & Biology*. 2017/09/20 2017;62(19):7814. doi:10.1088/1361-6560/aa8851

53. Wiesinger F, Bylund M, Yang J, et al. Zero TE-based pseudo-CT image conversion in the head and its application in PET/MR attenuation correction and MR-guided radiation therapy planning. *Magnetic Resonance in Medicine*. 2018/10/01 2018;80(4):1440-1451. doi:https://doi.org/10.1002/mrm.27134

54. Boulanger M, Nunes J-C, Chourak H, et al. Deep learning methods to generate synthetic CT from MRI in radiotherapy: A literature review. *Physica Medica*. 2021/09/01/ 2021;89:265-281. doi:https://doi.org/10.1016/j.ejmp.2021.07.027

55. Spadea MF, Maspero M, Zaffino P, Seco J. Deep learning based synthetic-CT generation in radiotherapy and PET: A review. *Medical Physics*. 2021/11/01 2021;48(11):6537-6566. doi:https://doi.org/10.1002/mp.15150

56. Park JM, Kim J-i, Park S-Y, Oh DH, Kim S-T. Reliability of the gamma index analysis as a verification method of volumetric modulated arc therapy plans. *Radiation Oncology*. 2018/09/14 2018;13(1):175. doi:10.1186/s13014-018-1123-x

57. Wiesinger F, Sacolick LI, Menini A, et al. Zero TE MR bone imaging in the head. *Magnetic Resonance in Medicine*. 2016/01/01 2016;75(1):107-114. doi:https://doi.org/10.1002/mrm.25545

58. Chopra KL, Leo P, Kabat C, et al. Evaluation of dose calculation accuracy of treatment planning systems in the presence of tissue heterogeneities. *Therapeutic Radiology and Oncology*. 2018;2

59. Das IJ, Cheng C-W, Cao M, Johnstone PAS. Computed tomography imaging parameters for inhomogeneity correction in radiation treatment planning. *Journal of Medical Physics*. 2016;41(1)

60. Kim J, Miller B, Siddiqui MS, Movsas B, Glide-Hurst C. FMEA of MR-Only Treatment Planning in the Pelvis. *Advances in Radiation Oncology*. 2019/01/01/ 2019;4(1):168-176. doi:https://doi.org/10.1016/j.adro.2018.08.024

61. Marques ML, da Silva NP, van der Heijde D, et al. Hounsfield Units measured in low dose CT reliably assess vertebral trabecular bone density changes over two years in axial spondyloarthritis. *Seminars in Arthritis and Rheumatism*. 2023/02/01/ 2023;58:152144. doi:https://doi.org/10.1016/j.semarthrit.2022.152144

62. Bibb R, Eggbeer D, Paterson A. *Medical Modelling: The Application of Advanced Design and Rapid Prototyping Techniques in Medicine*. Elsevier Science; 2014.

63. Jiang DZ, Dai ZT, Bao ZR, et al. CT value organ and homogeneous assigned methods-based radiation treatment planning of pelvic cavity tumors. *Int-J-Radiat-Res*. 2019;17(4):667-674.

64. Uh J, Merchant TE, Li Y, Li X, Hua C. MRI-based treatment planning with pseudo CT generated through atlas registration. *Medical Physics*. 2014/05/01 2014;41(5):051711. doi:https://doi.org/10.1118/1.4873315

65. Burgos N, Cardoso JM, Thielemans K, et al. Attenuation Correction Synthesis for Hybrid PET-MR Scanners: Application to Brain Studies. *IEEE Transactions on Medical Imaging*. 2014:2332-2341. doi:10.1109/TMI.2014.2340135

66. Dowling JA, Sun J, Pichler P, et al. Automatic Substitute Computed Tomography Generation and Contouring for Magnetic Resonance Imaging (MRI)-Alone External Beam Radiation Therapy From Standard MRI Sequences. *International Journal of Radiation Oncology*Biology*Physics*. 2015/12/01/ 2015;93(5):1144-1153. doi:https://doi.org/10.1016/j.ijrobp.2015.08.045

67. Kim J, Glide-Hurst C, Doemer A, Wen N, Movsas B, Chetty IJ. Implementation of a Novel Algorithm For Generating Synthetic CT Images From Magnetic Resonance Imaging Data Sets for Prostate Cancer Radiation Therapy. *International Journal of Radiation Oncology*Biology*Physics*. 2015/01/01/ 2015;91(1):39-47. doi:https://doi.org/10.1016/j.ijrobp.2014.09.015

68. Sjölund J, Forsberg D, Andersson M, Knutsson H. Generating patient specific pseudo-CT of the head from MR using atlas-based regression. *Physics in Medicine & Biology*. 2015/01/07 2015;60(2):825. doi:10.1088/0031-9155/60/2/825

69. Gudur MSR, Hara W, Le Q-T, Wang L, Xing L, Li R. A unifying probabilistic Bayesian approach to derive electron density from MRI for radiation therapy treatment planning. *Physics in Medicine & Biology*. 2014/10/16 2014;59(21):6595. doi:10.1088/0031-9155/59/21/6595

70. Dowling JA, Lambert J, Parker J, et al. An Atlas-Based Electron Density Mapping Method for Magnetic Resonance Imaging (MRI)-Alone Treatment Planning and Adaptive MRI-Based Prostate Radiation Therapy. *International Journal of Radiation Oncology*Biology*Physics*. 2012/05/01/ 2012;83(1):e5-e11. doi:https://doi.org/10.1016/j.ijrobp.2011.11.056

71. Demol B, Boydev C, Korhonen J, Reynaert N. Dosimetric characterization of MRI-only treatment planning for brain tumors in atlas-based pseudo-CT images generated from standard T1-weighted MR images. *Medical Physics*. 2016/12/01 2016;43(12):6557-6568. doi:https://doi.org/10.1118/1.4967480

72. Guerreiro F, Burgos N, Dunlop A, et al. Evaluation of a multi-atlas CT synthesis approach for MRI-only radiotherapy treatment planning. *Physica Medica*. 2017/03/01/ 2017;35:7-17. doi:https://doi.org/10.1016/j.ejmp.2017.02.017

73. Andreasen D, Van Leemput K, Edmund JM. A patch-based pseudo-CT approach for MRI-only radiotherapy in the pelvis. *Medical Physics*. 2016/08/01 2016;43(8Part1):4742-4752. doi:https://doi.org/10.1118/1.4958676

74. Wyatt JJ, Dowling JA, Kelly CG, et al. Investigating the generalisation of an atlas-based synthetic-CT algorithm to another centre and MR scanner for prostate MR-only radiotherapy. *Physics in Medicine & Biology*. 2017/11/21 2017;62(24):N548. doi:10.1088/1361-6560/aa9676

75. Farjam R, Tyagi N, Deasy JO, Hunt MA. Dosimetric evaluation of an atlas-based synthetic CT generation approach for MR-only radiotherapy of pelvis anatomy. *Journal of Applied Clinical Medical Physics*. 2019/01/01 2019;20(1):101-109. doi:https://doi.org/10.1002/acm2.12501

76. Figueiredo M. *On Gaussian Radial Basis Function Approximations: Interpretation, Extensions, and Learning Strategies*. vol 2. 2000:2618-2621.

77. Biau G, Scornet E. A random forest guided tour. *TEST*. 2016/06/01 2016;25(2):197-227. doi:10.1007/s11749-016-0481-7

78. Ghose S, Dowling JA, Rai R, Liney GP. Substitute CT generation from a single ultra short time echo MRI sequence: preliminary study. *Physics in Medicine & Biology*. 2017/03/17 2017;62(8):2950. doi:10.1088/1361-6560/aa508a

79. Johansson A, Karlsson M, Nyholm T. CT substitute derived from MRI sequences with ultrashort echo time. *Medical Physics*. 2011/05/01 2011;38(5):2708-2714. doi:https://doi.org/10.1118/1.3578928

80. Huynh T, Gao Y, Kang J, et al. Estimating CT Image From MRI Data Using Structured Random Forest and Auto-Context Model. *IEEE Transactions on Medical Imaging*. 2016;35(1):174-183. doi:10.1109/TMI.2015.2461533

81. Largent A, Nunes JC, Saint-Jalmes H, et al. Pseudo-CT generation by conditional inference random forest for MRI-based radiotherapy treatment planning. 2017:46-50.

82. Walston SL, Seki H, Takita H, et al. Data set terminology of deep learning in medicine: a historical review and recommendation. *Japanese Journal of Radiology*. 2024/06/10 2024;doi:10.1007/s11604-024-01608-1

83. Goodfellow IB, Yoshia; Courville, Aaron. *Deep Learning*. MIT Press; 2016.

84. Gui J, Sun Z, Wen Y, Tao D, Ye J. A Review on Generative Adversarial Networks: Algorithms, Theory, and Applications. *IEEE Transactions on Knowledge and Data Engineering*. 2023;35(4):3313-3332. doi:10.1109/TKDE.2021.3130191

85. Lombardi AF, Ma Y-J, Jang H, et al. Synthetic CT in Musculoskeletal Disorders: A Systematic Review. *Investigative Radiology*. 2023;58(1)

86. Sindhura DN, Pai RM, Bhat SN, Pai MMM. A review of deep learning and Generative Adversarial Networks applications in medical image analysis. *Multimedia Systems*. 2024/05/28 2024;30(3):161. doi:10.1007/s00530-024-01349-1

87. Wang C, Uh J, Merchant TE, Hua C-h, Acharya S. Facilitating MR-Guided Adaptive Proton Therapy in Children Using Deep Learning-Based Synthetic CT. *International Journal of Particle Therapy*. 2022/01/01/ 2022;8(3):11-20. doi:https://doi.org/10.14338/IJPT-20-00099.1

88. Zhao S, Geng C, Guo C, Tian F, Tang X. SARU: A self-attention ResUNet to generate synthetic CT images for MR-only BNCT treatment planning. *Medical Physics*. 2023/01/01 2023;50(1):117-127. doi:https://doi.org/10.1002/mp.15986

89. Koike Y, Akino Y, Sumida I, et al. Feasibility of synthetic computed tomography generated with an adversarial network for multi-sequence magnetic resonance-based brain radiotherapy. *Journal of Radiation Research*. 2020;61(1):92-103. doi:10.1093/jrr/rrz063

90. Olberg S, Zhang H, Kennedy WR, et al. Synthetic CT reconstruction using a deep spatial pyramid convolutional framework for MR-only breast radiotherapy. *Medical Physics*. 2019/09/01 2019;46(9):4135-4147. doi:https://doi.org/10.1002/mp.13716

91. Zhou X, Cai W, Cai J, et al. Multimodality MRI synchronous construction based deep learning framework for MRI-guided radiotherapy synthetic CT generation. *Computers in Biology and Medicine*. 2023/08/01/ 2023;162:107054. doi:https://doi.org/10.1016/j.compbiomed.2023.107054

92. Zhao Y, Wang H, Yu C, et al. Compensation cycle consistent generative adversarial networks (Comp-GAN) for synthetic CT generation from MR scans with truncated anatomy. *Medical Physics*. 2023/07/01 2023;50(7):4399-4414. doi:https://doi.org/10.1002/mp.16246

93. Liu Y, Lei Y, Wang Y, et al. MRI-based treatment planning for proton radiotherapy: dosimetric validation of a deep learning-based liver synthetic CT generation method. *Physics in Medicine & Biology*. 2019/07/16 2019;64(14):145015. doi:10.1088/1361-6560/ab25bc

94. Hsu S-H, Han Z, Leeman JE, Hu Y-H, Mak RH, Sudhyadhom A. Synthetic CT generation for MRI-guided adaptive radiotherapy in prostate cancer. Original Research. *Frontiers in Oncology*. 2022;12

95. Wyatt JJ, Kaushik S, Cozzini C, et al. Comprehensive dose evaluation of a Deep Learning based synthetic Computed Tomography algorithm for pelvic Magnetic Resonance-only radiotherapy. *Radiotherapy and Oncology*. 2023/07/01/ 2023;184:109692. doi:https://doi.org/10.1016/j.radonc.2023.109692

96. Rippke C, Renkamp CK, Stahl-Arnsberger C, et al. A body mass index-based method for “MR-only” abdominal MR-guided adaptive radiotherapy. *Zeitschrift für Medizinische Physik*. 2023/02/08/ 2023;doi:https://doi.org/10.1016/j.zemedi.2022.12.001

97. Garcia Hernandez A, Fau P, Wojak J, et al. Synthetic computed tomography generation for abdominal adaptive radiotherapy using low-field magnetic resonance imaging. *Physics and Imaging in Radiation Oncology*. 2023/01/01/ 2023;25:100425. doi:https://doi.org/10.1016/j.phro.2023.100425

98. Lenkowicz J, Votta C, Nardini M, et al. A deep learning approach to generate synthetic CT in low field MR-guided radiotherapy for lung cases. *Radiotherapy and Oncology*. 2022/11/01/ 2022;176:31-38. doi:https://doi.org/10.1016/j.radonc.2022.08.028

99. Bird D, Nix MG, McCallum H, et al. Multicentre, deep learning, synthetic-CT generation for ano-rectal MR-only radiotherapy treatment planning. *Radiotherapy and Oncology*. 2021/03/01/ 2021;156:23-28. doi:https://doi.org/10.1016/j.radonc.2020.11.027

100. Avey G. Technical Improvements in Head and Neck MR Imaging: At the Cutting Edge. *Neuroimaging Clinics of North America*. 2020/08/01/ 2020;30(3):295-309. doi:https://doi.org/10.1016/j.nic.2020.04.002

101. Tang B, Wu F, Fu Y, et al. Dosimetric evaluation of synthetic CT image generated using a neural network for MR-only brain radiotherapy. *Journal of Applied Clinical Medical Physics*. 2021/03/01 2021;22(3):55-62. doi:https://doi.org/10.1002/acm2.13176

102. Jabbarpour A, Mahdavi SR, Vafaei Sadr A, Esmaili G, Shiri I, Zaidi H. Unsupervised pseudo CT generation using heterogenous multicentric CT/MR images and CycleGAN: Dosimetric assessment for 3D conformal radiotherapy. *Computers in Biology and Medicine*. 2022/04/01/ 2022;143:105277. doi:https://doi.org/10.1016/j.compbiomed.2022.105277

103. Zhu M, Gong S, Qian Z, Zhang L. A Brief Review on Cycle Generative Adversarial Networks. *Proceedings of The 7th International Conference on Intelligent Systems and Image Processing 2019*. 2019;

104. Sun H, Xi Q, Fan R, et al. Synthesis of pseudo-CT images from pelvic MRI images based on an MD-CycleGAN model for radiotherapy. *Physics in Medicine & Biology*. 2022/01/28 2022;67(3):035006. doi:10.1088/1361-6560/ac4123

105. Reeder SB, Pineda AR, Wen Z, et al. Iterative decomposition of water and fat with echo asymmetry and least-squares estimation (IDEAL): Application with fast spin-echo imaging. *Magnetic Resonance in Medicine*. 2005/09/01 2005;54(3):636-644. doi:https://doi.org/10.1002/mrm.20624

106. Lerner M, Medin J, Jamtheim Gustafsson C, Alkner S, Siversson C, Olsson LE. Clinical validation of a commercially available deep learning software for synthetic CT generation for brain. *Radiation Oncology*. 2021/04/07 2021;16(1):66. doi:10.1186/s13014-021-01794-6

107. Ranta I, Wright P, Suilamo S, et al. Clinical feasibility of a commercially available MRI-only method for radiotherapy treatment planning of the brain. *Journal of Applied Clinical Medical Physics*. 2023/09/01 2023;24(9):e14044. doi:https://doi.org/10.1002/acm2.14044

108. Su K-H, Friel HT, Kuo J-W, et al. UTE-mDixon-based thorax synthetic CT generation. *Medical Physics*. 2019/08/01 2019;46(8):3520-3531. doi:https://doi.org/10.1002/mp.13574

109. Wang H, Chandarana H, Block KT, Vahle T, Fenchel M, Das IJ. Dosimetric evaluation of synthetic CT for magnetic resonance-only based radiotherapy planning of lung cancer. *Radiation Oncology*. 2017/06/26 2017;12(1):108. doi:10.1186/s13014-017-0845-5

110. Hsu S-H, Cao Y, Huang K, Feng M, Balter JM. Investigation of a method for generating synthetic CT models from MRI scans of the head and neck for radiation therapy. *Physics in Medicine & Biology*. 2013/11/11 2013;58(23):8419. doi:10.1088/0031-9155/58/23/8419

111. Bredfeldt JS, Liu L, Feng M, Cao Y, Balter JM. Synthetic CT for MRI-based liver stereotactic body radiotherapy treatment planning. *Physics in Medicine & Biology*. 2017/03/17 2017;62(8):2922. doi:10.1088/1361-6560/aa5059

112. Koivula L, Seppälä T, Collan J, Visapää H, Tenhunen M, Korhonen A. Synthetic computed tomography based dose calculation in prostate cancer patients with hip prostheses for magnetic resonance imaging-only radiotherapy. *Physics and Imaging in Radiation Oncology*. 2023/07/01/ 2023;27:100469. doi:https://doi.org/10.1016/j.phro.2023.100469

113. Jerban S, Ma Y, Jang H, et al. Water proton density in human cortical bone obtained from ultrashort echo time (UTE) MRI predicts bone microstructural properties. *Magnetic Resonance Imaging*. 2020/04/01/ 2020;67:85-89. doi:https://doi.org/10.1016/j.mri.2020.01.004

114. Segars WP, Mahesh M, Beck TJ, Frey EC, Tsui BMW. Realistic CT simulation using the 4D XCAT phantom. *Medical Physics*. 2008/08/01 2008;35(8):3800-3808. doi:https://doi.org/10.1118/1.2955743

115. Kim D-h, Adalsteinsson E, Spielman DM. Simple analytic variable density spiral design. *Magnetic Resonance in Medicine*. 2003/07/01 2003;50(1):214-219. doi:https://doi.org/10.1002/mrm.10493

116. Heberlein and K, Hu X. Auto-calibrated parallel spiral imaging. *Magnetic Resonance in Medicine*. 2006/03/01 2006;55(3):619-625. doi:https://doi.org/10.1002/mrm.20811

117. Lustig M, Pauly JM. SPIRiT: Iterative self-consistent parallel imaging reconstruction from arbitrary k-space. *Magnetic Resonance in Medicine*. 2010/08/01 2010;64(2):457-471. doi:https://doi.org/10.1002/mrm.22428

118. Engström M, McKinnon G, Cozzini C, Wiesinger F. In-phase zero TE musculoskeletal imaging. *Magnetic Resonance in Medicine*. 2020/01/01 2020;83(1):195-202. doi:https://doi.org/10.1002/mrm.27928

119. Brodsky EK, Holmes JH, Yu H, Reeder SB. Generalized k-space decomposition with chemical shift correction for non-cartesian water-fat imaging. *Magnetic Resonance in Medicine*. 2008/05/01 2008;59(5):1151-1164. doi:https://doi.org/10.1002/mrm.21580

120. Glover PM. Interaction of MRI field gradients with the human body. *Physics in Medicine & Biology*. 2009/10/14 2009;54(21):R99. doi:10.1088/0031-9155/54/21/R01

121. Czervionke LF, Daniels DL, Wehrli FW, et al. Magnetic susceptibility artifacts in gradient-recalled echo MR imaging. *American Journal of Neuroradiology*. 1988;9(6):1149.

122. Yan Y, Yang J, Li Y, Ding Y, Kadbi M, Wang J. Impact of geometric distortion on dose deviation for photon and proton treatment plans. *Journal of Applied Clinical Medical Physics*. 2022/03/01 2022;23(3):e13517. doi:https://doi.org/10.1002/acm2.13517

123. Kirsch S, Schad LR. Single-slice mapping of ultrashort T2. *Journal of Magnetic Resonance*. 2011/05/01/ 2011;210(1):133-136. doi:https://doi.org/10.1016/j.jmr.2011.02.003

124. Olson A, Phillips K, Eng T, et al. Assessing dose variance from immobilization devices in VMAT head and neck treatment planning: A retrospective case study analysis. *Medical Dosimetry*. 2018/03/01/ 2018;43(1):39-45. doi:https://doi.org/10.1016/j.meddos.2017.08.001

125. Hobson MA, Hu Y, Caldwell B, et al. AAPM Task Group 334: A guidance document to using radiotherapy immobilization devices and accessories in an MR environment. *Medical Physics*. 2024/06/01 2024;51(6):3822-3849. doi:https://doi.org/10.1002/mp.17061

126. Soliman AS, Burns L, Owrangi A, et al. A realistic phantom for validating MRI-based synthetic CT images of the human skull. *Medical Physics*. 2017/09/01 2017;44(9):4687-4694. doi:https://doi.org/10.1002/mp.12428

127. Chandramohan D, Cao P, Han M, et al. Bone material analogues for PET/MRI phantoms. *Medical Physics*. 2020/05/01 2020;47(5):2161-2170. doi:https://doi.org/10.1002/mp.14079

128. Audigier R, Lotufo R. Seed-Relative Segmentation Robustness of Watershed and Fuzzy Connectedness Approaches. 2007:61-70.

129. Wang S, Siskind JM. Image segmentation with minimum mean cut. 2001:517-524 vol.1.

130. Wang S, Siskind JM. Image segmentation with ratio cut. *IEEE Transactions on Pattern Analysis and Machine Intelligence*. 2003;25(6):675-690. doi:10.1109/TPAMI.2003.1201819

131. Jianbo S, Malik J. Normalized cuts and image segmentation. *IEEE Transactions on Pattern Analysis and Machine Intelligence*. 2000;22(8):888-905. doi:10.1109/34.868688

132. Bejar HHC, Ferzoli Guimaraes SJ, Miranda PAV. Efficient hierarchical graph partitioning for image segmentation by optimum oriented cuts. *Pattern Recognition Letters*. 2020/03/01/ 2020;131:185-192. doi:https://doi.org/10.1016/j.patrec.2020.01.008

133. Ester M, Kriegel H-P, Sander J, Xu X. A density-based algorithm for discovering clusters in large spatial databases with noise. 1996:226-231.

134. Campello RJGB, Moulavi D, Sander J. Density-Based Clustering Based on Hierarchical Density Estimates. Springer Berlin Heidelberg; 2013:160-172.

135. Ankerst M, Breunig MM, Kriegel H-P, Sander J. OPTICS: ordering points to identify the clustering structure. presented at: Proceedings of the 1999 ACM SIGMOD international conference on Management of data; 1999; Philadelphia, Pennsylvania, USA. https://doi.org/10.1145/304182.304187

136. Tokuda EK, Comin CH, Costa LdF. Revisiting agglomerative clustering. *Physica A: Statistical Mechanics and its Applications*. 2022/01/01/ 2022;585:126433. doi:https://doi.org/10.1016/j.physa.2021.126433

137. Hsin-Chia C, Wei-Jung C, Sheng-Jyh W. Contrast-based color image segmentation. *IEEE Signal Processing Letters*. 2004;11(7):641-644. doi:10.1109/LSP.2004.830116

138. Autret D, Guilleminet C, Roussel A, Cossec-Kerloc'h E, Dufreneix S. Comparison of four synthetic CT generators for brain and prostate MR-only workflow in radiotherapy. *Radiation Oncology*. 2023/09/05 2023;18(1):146. doi:10.1186/s13014-023-02336-y

139. Tahri S, Texier B, Nunes J-C, et al. A deep learning model to generate synthetic CT for prostate MR-only radiotherapy dose planning: a multicenter study. Original Research. *Frontiers in Oncology*. 2023;13

140. Olthof S-C, Reinert C, Nikolaou K, et al. Detection of lung lesions in breath-hold VIBE and free-breathing Spiral VIBE MRI compared to CT. *Insights into Imaging*. 2021/11/24 2021;12(1):175. doi:10.1186/s13244-021-01124-0